Soft Matter

ARTICLE TYPE

Cite this: DOI: 00.0000/xxxxxxxxxx

Influence of myosin activity and mechanical impact on keratocyte polarization†

Adrian Moure*[a] and Hector Gomez[a,b,c]

Received Date
Accepted Date

DOI: 00.0000/xxxxxxxxxx

In cell migration, polarization is the process by which a stationary cell breaks symmetry and initiates motion. Although a lot is known about the mechanisms involved in cell polarization, the role played by myosin contraction remains unclear. In addition, cell polarization by mechanical impact has received little attention. Here, we study the influence of myosin activity on cell polarization and the initiation of motion induced by mechanical cues using a computational model for keratocytes. The model accounts for cell deformation, the dynamics of myosin and the signaling protein RhoA (a member of the Rho GTPases family), as well as the forces acting on the actomyosin network. Our results show that the attainment of a steady polarized state depends on the strength of myosin down- or up-regulation and that myosin upregulation favors cell polarization. Our results also confirm the existence of a threshold level for cell polarization, which is determined by the level of polarization of the Rho GTPases at the time the external stimuli vanish. In all, this paper shows that capturing the interactions between the signaling proteins (Rho GTPases for keratocytes) and the compounds of the motile machinery in a moving cell is crucial to study cell polarization.

1 Introduction

Cell migration is a limiting step of the metastatic cascade[1] and plays a pivotal role in tissue morphogenesis[2–4] and immune response[5,6]. Fish keratocytes constitute perhaps the simplest example of eukaryotic cell motility[7–13]. The keratocyte motile machinery consists of a 2D network of actin filaments which spreads over the cell and is attached to the substrate through adhesion proteins called integrins. The actin network displays a denser structure at the cell's front, called lamellipodium, which pushes the cell membrane forward. The forward protrusion is caused by the rapid polymerization of actin filaments beneath the membrane. Molecular motors myosin II induce the contraction of the actin network at the cell's rear. Moving keratocytes display a polarized state characterized by frontal protrusion and rear contraction. Not only keratocytes, but any moving cell exhibits a polarized state (also referred to as polarity) in which the components of the motile machinery distribute along the direction of motion according to their role. Cell polarization is the process by which a stationary cell breaks symmetry and the cytosolic compounds reorganize in an appropriate way that permits the initiation of cell motion.

Due to the pivotal role played in cell migration, the study of the mechanisms involved in cell polarization has drawn the attention of many researchers[13–20]. Some cells (e.g., keratocytes) spontaneously leave their stationary state and initiate motion in a process known as spontaneous cell polarization. The spontaneous polarization of a keratocyte is a multistep process in which the circular symmetry is broken by stochastic fluctuations of the actin network[18,21]. Yam and collaborators proposed a theoretical model in which spontaneous cell polarization starts with the retraction of the prospective cell's rear followed by the protrusion of the cell's front once the cell's rear has formed[20]. The authors postulated that keratocyte polarization is a process regulated by Rho GTPases and driven by myosin contraction. Most works that study spontaneous cell polarization agree that cell polarization involves the formation of the cell's rear first, is a myosin-driven process, and is affected by the cell-substrate adhesion strength[14,15,21,22]. In the case of cell polarization induced by external stimuli, the scenario is more complicated. The polarization of the cell usually starts in the region of the cell which initially perceives the stimulus. Cell polarization by external stimuli represents the most common situation and has been widely investigated in works that study chemotaxis[23], haptotaxis[24], and durotaxis[25]. Those works have mainly focused on the dynamics of the signaling proteins involved in cell polarization as well as the influence of the cell-substrate adhesion strength and the substrate compliance on cell

---

[a] *School of Mechanical Engineering, Purdue University, West Lafayette, 47907 IN, USA. E-mail: amourero@purdue.edu*
[b] *Weldon School of Biomedical Engineering, Purdue University, West Lafayette, 47907 IN, USA.*
[c] *Purdue University Center for Cancer Research, Purdue University, West Lafayette, 47906 IN, USA.*

† Electronic Supplementary Information (ESI) available: Supporting figures and videos illustrating the simulation results. See DOI: 10.1039/cXsm00000x/

polarization. The initiation of motion induced by mechanical impact represents an outstanding example of cell polarization by external stimulus. Verkhovsky and collaborators showed that not only cell-cell collisions, but also an external pressure applied on the cell's boundary is enough to provoke the initiation of motion of keratocytes[13]. In that case, polarization begins with the forward displacement of the cell's rear caused by the external pressure. Cell polarization by mechanical impact is also observed in keratocytes with inhibited myosin activity[13].

Although the cell migration community agrees that spontaneous cell polarization involves the formation of the cell's rear first, there is no consensus on the mechanism that drives the formation of the cell's rear: whether it is caused by an increase of myosin contraction[14] or an increase of the actin depolymerization rate[16] remains unanswered. Different authors conducted experiments of keratocyte polarization with different levels of myosin down- and up-regulation[13,20]. The results are different, probably as a result of different experimental conditions. Myosin inhibition does not affect cell polarization in ref.[13], whereas myosin inhibition decreases the fraction of cells that polarize in ref.[20]. Likewise, ref.[20] could not explain why spatially-localized upregulation of myosin activity induces cell polarization but spatially-localized downregulation does not. These discrepancies prove that the role played by myosin activity on cell polarization remains unclear. Some works suggest that the cell must display a minimum level of polarization at the time the stimulus ceases in order to attain a steady polarized state[13,21,26]. To the best of our knowledge, how to define that threshold for cell polarization remains an open question.

In this paper we address those questions and shed light into the mechanisms of cell polarization by means of a computational model. In particular, we focus on the influence of myosin activity on cell polarization and the initiation of motion induced by mechanical cues. We propose a mathematical model for 2D keratocyte migration. We use the phase-field method[27–29] to capture the cell's deformation and motion. We consider the dynamics of the signaling protein RhoA, which is a member of the Rho GTPases family associated to the contraction of the cell's rear. Rho GTPases proteins transition between an active membrane-bound form and an inactive cytosolic form. We use the wave-pinning (WP) model[30] to account for the dynamics of RhoA. We also account for the dynamics of myosin II (hereinafter, myosin) and the dynamics of the actin network. We assume the actin network behaves as a viscous fluid governed by a Stokes equation. We augment the Stokes equation with the forces caused by the motile machinery, i.e., myosin contraction, actin protrusion, cell-substrate adhesion, and membrane surface tension. We consider the presence of obstacles in the extracellular environment. We model the interaction between the cell and the obstacles through a repulsive force acting on the membrane. The repulsive force allows us to reproduce cell polarization by mechanical impact. Our model features several advantages that make it suitable to analyze cell polarization including the strong coupling between cell shape, cell motion, and polarization. References[31–33] used the WP model to compare the dynamics of Rho GTPases on different cell geometries, though the geometries were pre-defined and remained fixed. Their results showed that the cell shape can alter the dynamics of the Rho GTPases. Our model displays a more realistic picture in which the cell geometry is an unknown of the problem and evolves with time. Other works used the WP model on moving cells[34–36]. In most of those works, however, the WP model accounts for the dynamics of the compounds of the motile machinery (e.g., G-actin and F-actin), bypassing the interaction between the signaling proteins and the motile machinery compounds. Here, we consider the dynamics of both the signaling proteins (RhoA) and the molecular motors (myosin) and assume that active RhoA promotes myosin association. Computational models usually assume that the active and inactive forms of Rho GTPases proteins distribute throughout the cytosol (see, e.g., refs.[37,38]). An accurate description of the Rho GTPases dynamics requires that the active form is located on the cell membrane and the inactive form is located in the cytosol. We capture the dynamics of the active membrane-bound and the inactive cytosolic forms of RhoA to the membrane and the cytosol, respectively, by using the phase-field method. Finally, although other works have computationally studied the mechanisms of spontaneous cell polarization[21], we believe the paper presented here is the first computational work that reproduces and studies cell polarization by mechanical impact.

Our model provides insight in the interplay between cell geometry, Rho GTPases proteins, and myosin-induced contraction during cell polarization. Our model results explain the differences between the experiments in ref.[13] and ref.[20], suggesting that ref.[13] and ref.[20] analyzed keratocytes with different levels of myosin inhibition. Our results also show that myosin-induced contraction favors cell polarization, which explains why spatially-localized downregulation of myosin activity does not induce cell polarization[20]. Our model results successfully reproduce cell polarization by mechanical impact and suggest that myosin contraction is required for cell polarization by mechanical cues. Finally, the results reported here confirm the existence of a threshold level for cell polarization, which is determined by the level of polarization of the Rho GTPases at the time the external stimuli vanish. We conclude that coupling the dynamics of the signaling proteins (Rho GTPases for keratocytes) and the compounds of the motile machinery with cell shape is crucial to study cell polarization.

2 Model description

We propose a 2D model for keratocyte polarization and migration on rigid substrates in the presence of obstacles. We organize the model into four coupled modules. First, we capture the cell's shape and motion by using the phase-field method. Second, we consider a generic signaling protein that transitions between an active membrane-bound state and a passive cytosolic state. In particular, we consider RhoA (also known as Rho), a member of the Rho GTPases family. The third module accounts for the dynamics of the molecular motor myosin II. The final module includes a force-balance equation to capture the dynamics of the actomyosin network, which is assumed to behave as a viscous fluid. We explain the four modules and their interactions in the following paragraphs (an overview of the model may be found in Fig. 1).

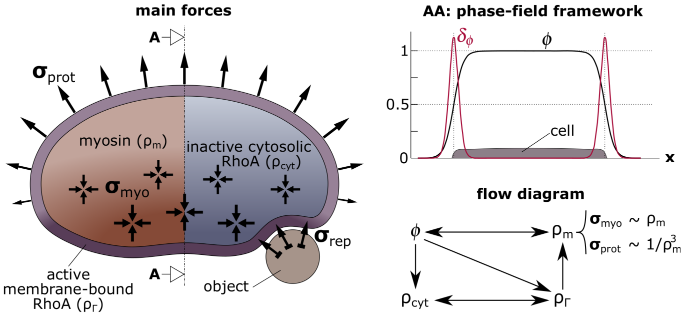

Fig. 1 Conceptual phase-field model of keratocyte migration. On the left, main forces acting on the actomyosin network (actin protrusion, myosin contraction, and object-induced repulsion). On the right-top, description of the phase-field framework used in the model to capture the cell (ϕ) and the membrane (δ_ϕ). On the right-bottom, flow diagram describing the interactions between the components of the model and the main forces. Cell geometry (ϕ) affects the distribution of the cytosolic and membrane-bound compounds. RhoA dynamics is controlled by the wave-pinning model. Active RhoA promotes myosin association. Myosin dictates cell motion by means of protrusion and contraction.

2.1 Phase-field approach. Cell motion

We use the phase-field variable $\phi(\boldsymbol{x},t)$ to capture the cell's shape and motion. The use of the phase-field method allows us to pose the problem on a fixed domain and solve it using a single fixed mesh. The phase field ϕ smoothly transitions from 0 outside the cell to 1 inside the cell; see Fig. 1-right. We assume that the cell's membrane (i.e., the interface) deforms following the actin network flow. We denote the velocity of the actin network as $\boldsymbol{u}(\boldsymbol{x},t)$; see Section 2.4 for more details. The phase-field equation that governs the motion of the cell is written as

$$\frac{\partial \phi}{\partial t} + \boldsymbol{u} \cdot \nabla \phi = \Gamma_\phi \left(\varepsilon \nabla^2 \phi - \frac{G'(\phi)}{\varepsilon} + c\varepsilon |\nabla \phi| \right), \tag{1}$$

where Γ_ϕ and ε are parameters, $c = -\nabla \cdot (\nabla\phi/|\nabla\phi|)$ is the curvature of the membrane, and $G(\phi) = 18\phi^2(1-\phi)^2$ is a double-well potential with minima at 0 and 1. The parameters Γ_ϕ and ε control the strength of the right-hand side of the equation and the width of the interface, respectively. Equation (1) may be interpreted as a level set equation that moves the interface with velocity $\boldsymbol{u}$, while the right-hand side of Eq. (1) imposes a hyperbolic tangent profile on the interface; see refs.[29,39,40] for more details.

We define the membrane marker δ_ϕ as a function of ϕ, such that $\delta_\phi = 2G(\phi)/\varepsilon$; see Fig. 1-right. The marker δ_ϕ is a smooth function that takes the value 1 on the interface and 0 elsewhere. We use δ_ϕ to localize the dynamics and reactions of certain compounds to the membrane[29,41,42], as we show in the following sections. The use of the membrane marker allows us to reformulate surface partial-differential equations (PDEs) defined on the membrane in curvilinear coordinates as equations in Cartesian coordinates on a box that encloses the cell.

2.2 RhoA dynamics

Rho GTPases are signaling proteins involved in cell motility[‡] [43–45]. These proteins cycle between active membrane-bound and inactive cytosolic forms. In a motile cell, Rho GTPases exhibit a non-uniform (i.e., polarized) distribution along the direction of motion. The non-uniform Rho GTPases distribution is usually induced by external stimuli such as, e.g., chemical or mechanical cues, although some cells can polarize in the absence of external stimuli in a process known as spontaneous cell polarization. Rho GTPases proteins in the active form accumulate at the front or rear edge of the cell (depending on their function) and trigger a response downwards in the signaling pathway. This response induces contraction at the rear and protrusion at the front, i.e., produces the polarization and subsequent motion of the cell. For this reason, Rho GTPases are key regulators of cell motility.

Here, we focus on RhoA, which is associated with myosin-induced contraction at the cell's rear[46,47]. We use the WP model[30] to account for the dynamics of RhoA. The WP model was originally proposed to reproduce the behavior of the Rho GTPases proteins. The original model coupled two 1D equations in Cartesian coordinates. Here, we propose an extension of the model that assumes the dynamics of the inactive form happens in the cytosol while the dynamics of the membrane-bound form of RhoA occurs on the membrane. The active and inactive forms of RhoA interact through boundary conditions on the cell's membrane and are also tightly coupled with the geometry of the cell through global mass-conservation constraints. A standard formulation of this problem would require moving volumetric and surface meshes that are compatible at the cell's membrane. By using the phase-field method (see, e.g., ref.[41]) we can reformulate the problem as a set of two equations in Cartesian coordinates that are solved on a box that encloses the cell. If we denote the active membrane-bound and inactive cytosolic forms of RhoA as $\rho_\Gamma(\boldsymbol{x},t)$ and $\rho_{cyt}(\boldsymbol{x},t)$, respectively, our extended WP model may be written as

$$\frac{\partial(\delta_\phi \rho_\Gamma)}{\partial t} = \nabla \cdot \left(D_\Gamma \delta_\phi \nabla \rho_\Gamma \right) + \delta_\phi f_\rho(\rho_\Gamma, \rho_{cyt}), \tag{2}$$

$$\frac{\partial(\phi \rho_{cyt})}{\partial t} = \nabla \cdot \left(D_{cyt} \phi \nabla \rho_{cyt} \right) - \delta_\phi f_\rho(\rho_\Gamma, \rho_{cyt}), \tag{3}$$

where we used the phase-field framework to pose the equations in the membrane and the cytosol with the markers δ_ϕ and ϕ, respectively. Note that the reaction term f_ρ in Eq. (3) is localized with the marker δ_ϕ because the transformation between ρ_Γ and ρ_{cyt} occurs on the membrane. D_Γ and D_{cyt} are the diffusion coefficients for ρ_Γ and ρ_{cyt}, respectively. Eqs. (2) and (3) do not include the advection produced by the velocity $\boldsymbol{u}$ because RhoA proteins are not bound to the actin filaments. Mori et al.[30] derived the WP model making three assumptions: (1) The total amount of RhoA is conserved, i.e., $\int_\Omega (\delta_\phi \rho_\Gamma + \phi \rho_{cyt})\, \mathrm{d}\Omega = N_\rho$ for all t, where N_ρ is constant; (2) ρ_Γ and ρ_{cyt} have different rates of diffusion such that $D_{cyt} >> D_\Gamma$; (3) the transition between ρ_Γ and ρ_{cyt} is dictated by a nonlinear relation which allows for bistabiliy of the active form of RhoA (i.e., ρ_Γ). The nonlinear function $f_\rho(\rho_\Gamma, \rho_{cyt})$

[‡] Cdc42, Rac, and RhoA are the main proteins of the Rho GTPases family.

proposed in[30] is

$$f_\rho(\rho_\Gamma, \rho_{\mathrm{cyt}}) = \left(k_0 + \gamma \frac{{\rho_\Gamma}^2}{K^2 + {\rho_\Gamma}^2}\right)\rho_{\mathrm{cyt}} - \eta\rho_\Gamma, \tag{4}$$

where k_0, γ, K, and η are constants. The function f_ρ controls the behavior of the WP model. We plotted f_ρ in the plane $(\rho_\Gamma, \rho_{\mathrm{cyt}})$ in Fig. 2-top and f_ρ as a function of ρ_Γ for three different values of ρ_{cyt} in Fig. 2-bottom (more details below). We plotted the graphs in Fig. 2 with the parameter values listed in Table 1. Only in this section to explain the function f_ρ, we neglect cell deformation and use the condition $D_{\mathrm{cyt}} >> D_\Gamma$ to assume that (i) ρ_{cyt} displays a uniform distribution in the cell and (ii) Eq. (2) can be written as $\partial\rho_\Gamma/\partial t = f_\rho$. Based on these assumptions, if $f_\rho < 0$, ρ_Γ tends to decrease and vice versa. The arrows plotted in Fig. 2-top indicate the tendency of ρ_Γ to increase or decrease for a constant ρ_{cyt}. Thus, the red dotted lines in Fig. 2-top represent stable ρ_Γ densities for a constant ρ_{cyt}. In Fig. 2-top, we divided the diagram f_ρ in three regions depending on the value of ρ_{cyt}. Regions I, II, and III comprise the points $(\rho_\Gamma, \rho_{\mathrm{cyt}})$ such that $\rho_{\mathrm{cyt}} < \rho^{\mathrm{I}}_{\mathrm{cyt}}$, $\rho^{\mathrm{I}}_{\mathrm{cyt}} < \rho_{\mathrm{cyt}} < \rho^{\mathrm{II}}_{\mathrm{cyt}}$, and $\rho_{\mathrm{cyt}} > \rho^{\mathrm{II}}_{\mathrm{cyt}}$, respectively, where $\rho^{\mathrm{I}}_{\mathrm{cyt}}$ and $\rho^{\mathrm{II}}_{\mathrm{cyt}}$ are constant values defined in the figure. The green dash-dotted lines represent the boundary between those regions. In regions I and III, f_ρ displays a single zero for a constant ρ_{cyt}, which represents a stable ρ_Γ density. In region II, f_ρ exhibits three zeros for a constant ρ_{cyt}. Two of those zeros represent stable ρ_Γ densities, while the other one represents an unstable density. Therefore, f_ρ exhibits two stability lines (the red dotted lines in the figure). One line is associated with low ρ_Γ densities and spreads along regions I and II. The other line is associated with high ρ_Γ densities and is located in regions II and III. In Fig. 2-bottom, we plotted f_ρ as a function of ρ_Γ for $\rho_{\mathrm{cyt}} = \rho^{\mathrm{I}}_{\mathrm{cyt}}$ (left), $\rho_{\mathrm{cyt}} = \rho_{\mathrm{cyt,A}}$ (center), and $\rho_{\mathrm{cyt}} = \rho^{\mathrm{II}}_{\mathrm{cyt}}$ (right), where the value $\rho_{\mathrm{cyt,A}}$ is given in Fig. 2-top. $f_\rho(\rho_\Gamma, \rho^{\mathrm{I}}_{\mathrm{cyt}})$ and $f_\rho(\rho_\Gamma, \rho^{\mathrm{II}}_{\mathrm{cyt}})$ represent the transition between regions I and II, and II and III, respectively. Due to this fact, $f_\rho(\rho_\Gamma, \rho^{\mathrm{I}}_{\mathrm{cyt}})$ and $f_\rho(\rho_\Gamma, \rho^{\mathrm{II}}_{\mathrm{cyt}})$ display two zeros, one stable and the other one unstable. $f_\rho(\rho_\Gamma, \rho_{\mathrm{cyt,A}})$ represents a generic plot of region II, where we can observe the two stable ρ_Γ densities. Therefore, the simplified system based on assumptions (i) and (ii) can display bistability (coexistence of two stable ρ_Γ densities) if ρ_{cyt} is located in region II.

If assumptions (i) and (ii) do not hold, the behavior of the system is similar, though more complex. For instance, the front and rear edges of the cell may have different ρ_{cyt}. The pair $(\rho_\Gamma, \rho_{\mathrm{cyt}})$ at the front edge may be located on the stability line in region I (see Fig. 2-top), while $(\rho_\Gamma, \rho_{\mathrm{cyt}})$ at the rear edge may be located on the stability line in region III. In that case, the cell exhibits bistability despite ρ_{cyt} at the edges of the cell are not located in region II in the f_ρ diagram. More details about the behavior of the RhoA proteins can be found in Section 4.

The attainment of bistability and the number of patches of high ρ_Γ density also depends on the parameter values, the cell area, the membrane length, and the total amount of RhoA proteins considered. In our model, we considered a configuration of the cell and the parameter values such that the cell can attain bistability. Several authors have studied the influence of all of these factors on simplified versions of the WP model[30,48,49]. A detailed description of the influence of these factors is beyond the scope of this paper.

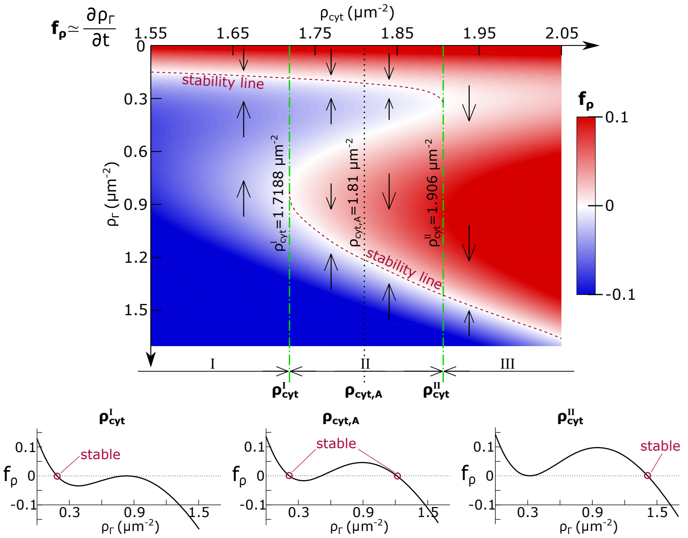

Fig. 2 Stability function $f_\rho(\rho_\Gamma, \rho_{\mathrm{cyt}})$ of the wave-pinning model. On the top, f_ρ as a function of ρ_Γ and ρ_{cyt}. The plot is divided in regions I, II, and III according to the number of zeros for a constant ρ_{cyt}. Green dash-dotted lines indicate the boundaries between regions, located at $\rho_{\mathrm{cyt}} = \rho^{\mathrm{I}}_{\mathrm{cyt}}$ and $\rho_{\mathrm{cyt}} = \rho^{\mathrm{II}}_{\mathrm{cyt}}$. Arrows indicate the tendency of ρ_Γ to increase or decrease for a constant ρ_{cyt}. Red dashed lines (stability lines) represent the stable ρ_Γ densities. One stability line is observed in regions I and III, while two stability lines coexist in region II. On the bottom, f_ρ as a function of ρ_Γ for three representative values of ρ_{cyt}, namely, $\rho^{\mathrm{I}}_{\mathrm{cyt}}$ (left), $\rho_{\mathrm{cyt,A}}$ (center), and $\rho^{\mathrm{II}}_{\mathrm{cyt}}$ (right).

2.3 Myosin dynamics

Myosin II is a molecular motor that can exert forces on the F-actin network and carry loads along the filaments. Myosin can be found attached to the F-actin network (associated) or diffused throughout the cytosol (dissociated). We denote the density of associated and dissociated myosin as $\rho_m(\boldsymbol{x},t)$ and $\rho^\star_m(\boldsymbol{x},t)$, respectively. We simplify myosin dynamics by assuming that there is a pool of dissociated myosin uniformly distributed throughout the cell[13,36]. We also assume that the total amount of myosin is conserved, i.e., $\int_\Omega \phi(\rho_m + \rho^\star_m)\,\mathrm{d}\Omega = N_m$, where N_m is the total amount of myosin, which is constant. Therefore, $\rho^\star_m$ is a function of time alone and can be computed as

$$\rho^\star_m(t) = \frac{N_m - \int_\Omega \phi\rho_m\,\mathrm{d}\Omega}{\int_\Omega \phi\,\mathrm{d}\Omega}. \tag{5}$$

We propose a reaction-diffusion equation for the dynamics of associated myosin, which is expressed as

$$\frac{\partial(\phi\rho_m)}{\partial t} + \nabla\cdot(\phi\rho_m\boldsymbol{u}) = \nabla\cdot(D_m\phi\nabla\rho_m) + b_m\phi\rho^\star_m - r_m\phi\rho_m + k_m\delta_\phi\rho^\star_m\rho_\Gamma, \tag{6}$$

where D_m is the diffusion coefficient and b_m, r_m, and k_m are the parameters of the reaction terms. Note that myosin advection, diffusion, and the b_m- and r_m-terms are localized to the cytosol with the marker ϕ, while the k_m-term is localized to the membrane with the marker δ_ϕ. In Eq. (6), the $\boldsymbol{u}$-term accounts for the motion of associated myosin caused by the flow of the actin network. The diffusive term accounts for the movement of myosin along the filaments (while attached to them). The b_m- and r_m-terms represent the association and dissociation of myosin to F-actin, where b_m and r_m are the association and dissociation rates, respectively. Finally, the k_m-term accounts for myosin association induced by the active membrane-bound form of RhoA. We assume that the activation rate is proportional to ρ_Γ. Equation (6) is analogous to the equations proposed in refs.[36,50] for associated myosin dynamics. The main difference lies in the k_m-term that we include to model RhoA-promoted myosin association.

2.4 F-actin network flow

We model the actin network as a Newtonian fluid governed by the Stokes equation. Following ref.[50], we neglect the pressure term. We augment the Stokes equation with the active (myosin contraction and actin protrusion) and passive forces arising from the motile machinery; see Fig. 1-left. The force-balance equation is expressed as

$$\nabla\cdot(\boldsymbol{\sigma}+\boldsymbol{\sigma}_{\text{myo}}+\boldsymbol{\sigma}_{\text{prot}}+\boldsymbol{\sigma}_{\text{rep}})+\boldsymbol{F}_{\text{mem}}+\boldsymbol{F}_{\text{vol}}+\boldsymbol{F}_{\text{adh}}=0, \qquad (7)$$

where $\boldsymbol{\sigma}=\mu\phi(\nabla\boldsymbol{u}+\nabla\boldsymbol{u}^T)$ is the viscous stress tensor localized to the cytosol. The parameter μ is the dynamic viscosity. We model the myosin-induced contraction of the actin network with the isotropic contractile stress $\boldsymbol{\sigma}_{\text{myo}}=\overline{\eta}_{\text{myo}}\phi\rho_m\boldsymbol{I}$, where $\boldsymbol{I}$ is the identity tensor and $\overline{\eta}_{\text{myo}}$ is a coefficient setting the strength of the contractile stress. The protrusive stress applied by the lamellipodium on the cell membrane takes the form $\boldsymbol{\sigma}_{\text{prot}}=-\eta_{\text{prot}}(\rho_m)\delta_{\text{prot}}\phi\nabla\phi\otimes\nabla\phi$, where the function $\eta_{\text{prot}}(\rho_m)$ controls the strength of the protrusive stress and the function δ_{prot} annihilates the protrusive stress in the vicinity of obstacles. We define $\eta_{\text{prot}}(\rho_m)=\frac{\overline{\eta}_{\text{prot}}}{1+\left(\rho_m/\rho_m^{\text{prot}}\right)^3}$, where $\overline{\eta}_{\text{prot}}$ and ρ_m^{prot} are parameters. This approach, in which protrusion is inversely proportional to myosin density, has been previously used in refs.[21,36,51]. We take $\delta_{\text{prot}}=\mathscr{H}(d_o(\boldsymbol{x})-d_{\text{prot}})$, where $\mathscr{H}$ is a smoothed-out Heaviside function[§], $d_o(\boldsymbol{x})$ is the distance between point $\boldsymbol{x}$ and the closest point to the object, and $d_{\text{prot}}=2.6\mu\text{m}$. The repulsive force $\nabla\cdot\boldsymbol{\sigma}_{\text{rep}}$ prevents the cell from penetrating the obstacles. We take $\boldsymbol{\sigma}_{\text{rep}}=\overline{\eta}_{\text{rep}}\delta_{\text{rep}}\phi\nabla\phi\otimes\nabla\phi$, where $\overline{\eta}_{\text{rep}}$ is a constant and the function $\delta_{\text{rep}}=\mathscr{H}(d_{\text{rep}}-d_\Gamma(\boldsymbol{x}))$ activates the repulsive stress in the vicinity of the obstacles, with $d_{\text{rep}}=1.7\mu\text{m}$. The function $d_\Gamma(\boldsymbol{x})$ is a constant extension of the distance field $d_o(\boldsymbol{x})$ at the membrane (i.e., at points $\boldsymbol{x}$ such that $\phi(\boldsymbol{x})=1/2$) in the normal direction to the membrane. The forces arising from the membrane configuration are the surface tension and the bending-energy force. These forces can be derived from the Helfrich free-energy for membranes[52,53] using the phase-field framework; the derivation may be found in ref.[54]. We neglect the force derived from the bending energy due to its small contribution to the cell's morphodynamics[54,55]. The force produced by the surface tension of the membrane is expressed as $\boldsymbol{F}_{\text{mem}}=-\gamma_\phi(\varepsilon\nabla^2\phi-G'(\phi)/\varepsilon)\nabla\phi$. The force $\boldsymbol{F}_{\text{mem}}$ is equivalent to $-\gamma_\phi c\boldsymbol{n}_{\Gamma_\phi}$, where γ_ϕ is the surface tension coefficient, c is the membrane curvature, and $\boldsymbol{n}_{\Gamma_\phi}$ is the normal vector to the cell membrane; see ref.[54]. We impose cell volume conservation through the force $\boldsymbol{F}_{\text{vol}}=\Lambda(A(t)-A_0)|\nabla\phi|\nabla\phi$, where Λ is a parameter, $A(t)=\int_\Omega\phi\,\mathrm{d}\Omega$ is the cell area (volume in 3D), and A_0 is the cell area at the initial time. $\boldsymbol{F}_{\text{vol}}$ allows for small changes in cell area[8]. Assuming that $\boldsymbol{F}_{\text{vol}}$ represents a pressure acting on the membrane caused by cell volume changes, we can establish a relation between the parameter Λ and the bulk modulus of the cytoplasm (more details in ref.[34]). Finally, we use a frictional drag force to model cell-substrate adhesion via integrin proteins. The adhesion force is written as $\boldsymbol{F}_{\text{adh}}=-\varsigma\phi\boldsymbol{u}$, where ς is the friction coefficient.

3 Numerical simulation

3.1 Numerical formulation

We solve the problem defined by Eqs. (1), (2), (3), (6), and (7) on a fixed domain by using Isogeometric Analysis (IGA). IGA is a generalization of the Finite Element Method (FEM) originally proposed in ref.[56]. IGA uses B-splines and NURBS (Non-Uniform Rational B-splines) as basis functions, which permits to overcome most of the drawbacks of classical FEM related to the spatial discretization of higher-order PDEs. Spaces constructed with B-splines possess arbitrary degree of continuity across element boundaries, among other notable properties[57–63]. The numerical formulation presented here is analogous to that explained in ref.[54]. We refer the reader to ref.[54] for a detailed description. We first derive the weak form of the problem by multiplying the equations with weighting functions and integrating in space. We consider periodic boundary conditions. After integrating by parts, we obtain the weak form of the problem. We next discretize in space by substituting the unknowns and the weighting functions by B-splines. We employ quadratic $\mathscr{C}^1$-continuous B-splines to guarantee that the Galerkin form is well defined.

We use the generalized-α method to integrate in time[70,71]. The time stepping scheme requires the solution of a non-linear system, which we solve by using the Newton–Raphson method. To avoid singularities, improve the condition number of the system, and speed up the numerics, we perform the following simplifications and substitutions:

(1) We only compute the c-term in Eq. (1) in the region comprised by the points $\boldsymbol{x}$ such that $|\nabla\phi|>10^{-8}$.

(2) We treat explicitly, rather than implicitly, the terms $\rho_m^\star$, δ_{rep}, and $A(t)$. As a result of the explicit discretization, these terms, which involve large computations, are constant during each time step.

(3) We replace the term $\varsigma\phi$ in $\boldsymbol{F}_{\text{adh}}$ by $\varsigma\phi+\varsigma_b$. ς_b is a basal friction coefficient such that $\varsigma >> \varsigma_b = 0.2\,\text{pN}\,\text{s}\,\mu\text{m}^{-3}$.

(4) Note that most of the unknowns approach to zero far from the cell and/or the membrane. In those regions, we modify the corresponding elements of the residual vector and the tangent matrix. A detailed description of this procedure may be found in ref.[54].

[§] In particular, we take $\mathscr{H}(x)=0.5+0.5\tanh(x/L_H)$, where $L_H=0.142\,857\mu\text{m}$.

Table 1 Parameter values used in the simulations.

Symbol	Description	Value	Units	Source
Γ_ϕ	Phase-field relaxation parameter	2.5	$\mu\mathrm{m}\,\mathrm{s}^{-1}$	Ref. [54]
ε	Phase-field interfacial length scale	2	$\mu\mathrm{m}$	Ref. [54]
D_Γ	Membrane-bound RhoA diffusion coefficient	0.1	$\mu\mathrm{m}^2\,\mathrm{s}^{-1}$	Ref. [30]
D_{cyt}	Cytosolic RhoA diffusion coefficient	10	$\mu\mathrm{m}^2\,\mathrm{s}^{-1}$	Ref. [30]
k_0	RhoA basal activation rate	0.075	s^{-1}	Ref. [30]
γ	RhoA maximal activation rate	1	s^{-1}	Ref. [30]
K	RhoA saturation parameter	1	$\mu\mathrm{m}^{-2}$	Ref. [30]
η	RhoA inactivation rate	1	s^{-1}	Ref. [30]
D_m	Myosin diffusion coefficient	0.9	$\mu\mathrm{m}^2\,\mathrm{s}^{-1}$	Ref. [64]
b_m	Actin-myosin association rate	5	s^{-1}	Ref. [65]
r_m	Actin-myosin dissociation rate	0.05	s^{-1}	Ref. [65]
k_m	RhoA-promoted myosin activation rate	60	$\mu\mathrm{m}^2\,\mathrm{s}^{-1}$	Estimated
μ	F-actin flow viscosity coefficient	500	$\mathrm{pN}\,\mathrm{s}\,\mu\mathrm{m}^{-1}$	Ref. [66]
$\overline{\eta}_{\mathrm{myo}}$	Strength of contractile forces	60	$\mathrm{pN}\,\mu\mathrm{m}$	Ref. [50]
$\overline{\eta}_{\mathrm{prot}}$	Strength of protrusive forces	812	$\mathrm{pN}\,\mu\mathrm{m}$	Ref. [35]
ρ_m^{prot}	Critical myosin density for actin protrusion	0.2382	$\mu\mathrm{m}^{-2}$	Estimated
d_{prot}	Effective distance for protrusion suppression	2.6	$\mu\mathrm{m}$	Ref. [67]
$\overline{\eta}_{\mathrm{rep}}$	Strength of repulsive forces	6000	$\mathrm{pN}\,\mu\mathrm{m}$	Ref. [67]
d_{rep}	Effective distance for obstacle detection	1.7	$\mu\mathrm{m}$	Ref. [67]
γ_ϕ	Cell membrane surface tension coefficient	12	pN	Ref. [68]
Λ	Strength of cell volume constraint	1.5	$\mathrm{pN}\,\mu\mathrm{m}^{-2}$	Estimated
ς	Cell-substrate friction coefficient	100	$\mathrm{pN}\,\mathrm{s}\,\mu\mathrm{m}^{-3}$	Refs. [50,69]

Points (1)–(4) speed up the numerics without introducing noticeable errors in the solution. The time stepping scheme moves forward to the next time step when the norm of the residual vectors associated with each unknown is reduced, at least, four orders of magnitude. We solve the problem in a periodic domain of $50 \times 50\mu\mathrm{m}^2$. We mesh the computational domain with 200×200 $\mathscr{C}^1$-continuous quadratic elements. We use a fixed time step of 0.05 s. We stop most simulations at $t = 300$ s. In some simulations, the cell has not achieved a steady state at $t = 300$ s. In those cases, we stop the simulations at $t = 600$ s. We developed the code used to run our simulations on top of the open source framework PetIGA[72]. PetIGA adds NURBS discretization capabilities to the scientific library PETSc[73].

3.2 Initial conditions and parameter values

Throughout the paper, we analyze several examples with different initial conditions. For the sake of simplicity, we define a generic initial condition as a function of the parameters ρ_Γ^-, ρ_Γ^+, ρ_{cyt}^-, ρ_{cyt}^+, ρ_m^-, and ρ_m^+. The initial conditions are defined as

$$\phi(\boldsymbol{x},0) = \phi_0(\boldsymbol{x}) = 0.5 - 0.5\tanh\left[\frac{2\sqrt{2}}{\varepsilon}\left(d_c(\boldsymbol{x}) - R_c\right)\right], \quad (8)$$

$$\delta_\phi(\boldsymbol{x},0) = \delta_{\phi 0}(\boldsymbol{x}) = 2G(\phi_0)/\varepsilon, \quad (9)$$

$$\rho_\Gamma(\boldsymbol{x},0) = \begin{cases} \rho_\Gamma^+\,\delta_{\phi 0}(\boldsymbol{x}) & \text{if } x \geq x_c, \\ \rho_\Gamma^-\,\delta_{\phi 0}(\boldsymbol{x}) & \text{if } x < x_c, \end{cases} \quad (10)$$

$$\rho_{\mathrm{cyt}}(\boldsymbol{x},0) = \begin{cases} \rho_{\mathrm{cyt}}^+[\phi_0(\boldsymbol{x})]^2 & \text{if } x \geq x_c, \\ \rho_{\mathrm{cyt}}^-[\phi_0(\boldsymbol{x})]^2 & \text{if } x < x_c, \end{cases} \quad (11)$$

$$\rho_m(\boldsymbol{x},0) = \begin{cases} \rho_m^+[\phi_0(\boldsymbol{x})]^2 & \text{if } x \geq x_c, \\ \rho_m^-[\phi_0(\boldsymbol{x})]^2 & \text{if } x < x_c, \end{cases} \quad (12)$$

$$\boldsymbol{u}(\boldsymbol{x},0) = 0, \quad (13)$$

where $G(\phi)$ is defined in Eq. (1), $R_c = 9\mu\mathrm{m}$ is the initial radius of the cell, and $d_c(\boldsymbol{x})$ is the distance to the cell's center $\boldsymbol{C} = (x_c, y_c)$. Unless otherwise stated, we take $x_c = y_c = 25\mu\mathrm{m}$, $\rho_\Gamma^- = \rho_\Gamma^+ = 0.22\mu\mathrm{m}^{-2}$, $\rho_{\mathrm{cyt}}^- = \rho_{\mathrm{cyt}}^+ = 1.997\mu\mathrm{m}^{-2}$, and $\rho_m^- = \rho_m^+ = 0.3\mu\mathrm{m}^{-2}$. The initial conditions of the problem are completely defined with the value of N_m. We take $N_m = 72.21$, which results from taking $\rho_m^- = \rho_m^+ = 0.3\mu\mathrm{m}^{-2}$ and a uniform $\rho_m^\star$ distribution of density $\rho_m^\star = 0.003\mu\mathrm{m}^{-2}$. Since we want to study the influence of myosin activity and mechanical impact on the mechanisms of cell polarization, we keep constant the total amount of RhoA $(N_\rho = 488.9)$ in all the examples except in the one shown in Section 4.1.3.

Note that we include the term ϕ_0^2, rather than ϕ_0, in Eqs. (11) and (12). If we define Eqs. (11) and (12) with the term ϕ_0, for certain values of the parameters ρ_Γ^-, ρ_Γ^+, ρ_{cyt}^-, ρ_{cyt}^+, ρ_m^-, and ρ_m^+, the initial conditions can be a solution of Eqs. (2), (3), and (6). In that case, the time stepping scheme cannot move forward because the residual vectors associated to those unknowns are zero at the initial time. Instead of modifying the convergence criteria at the first time step, we opted for including the term ϕ_0^2 so that the initial conditions are never a solution of Eqs. (2), (3), and (6).

Unless otherwise stated, the parameter values used in the different examples are listed in Table 1.

4 Results

In this section we present the model results that serve us to investigate the mechanisms of cell polarization. First, we analyze the main features of the model and the influence of the initial conditions. We next study the influence of myosin activity. Finally, we study different scenarios of cell polarization driven by mechanical impact. For the sake of clarity, we identify each simulation as *case capital letter-number*, where the capital letter refers to the subsection in which the simulation is shown. For instance, case A2 corresponds to a simulation shown in Section 4.1.

4.1 Basic features of the model: non-polarized and polarized initial conditions

Here, we present the main features of the model. We show that, in an isolated environment¶, only a cell with polarized initial conditions can initiate motion.

4.1.1 Non-polarized initial conditions

We first study a cell with non-polarized (i.e., circularly symmetric) initial conditions (case A0). In Fig. 3, we show the simulation results of case A0, in which we considered the parameter values and the initial conditions defined in Section 3.2. In Fig. 3a, we plotted the ρ_Γ and ρ_{cyt} distributions on the top row and the ρ_Γ and ρ_m distributions on the bottom row at times 0, 35, and 70 s. The arrows on the bottom row represent the velocity $\boldsymbol{u}$ at random locations inside the cell. In Fig. 3b, we plotted the time evolution of the cell area and perimeter. The non-polarized initial conditions exhibit low ρ_{cyt} and ρ_m densities‖ in the surroundings of the membrane (see $t = 0$ s in Fig. 3a), caused by the term ϕ_0^2 in Eqs. (11) and (12). This ρ_{cyt} and ρ_m perturbation near the membrane caused by the initial conditions vanishes after a few seconds. For this reason, the time evolution of the different parameters analyzed throughout the paper may exhibit a mild oscillation for $t \lesssim 5$ s; see, e.g., Fig. 3b. To reduce the visual impact of this oscillation in the graphs, we plotted the time evolution of the different parameters starting from $t = 0.2$ s. Figures. 3a and b show that the cell does not polarize (i.e., the cell keeps its circular symmetry) or initiate motion and attains a steady state at $t \approx 70$ s. At the steady state, the distributions of ρ_{cyt} and ρ_m are roughly uniform and the actin network displays centripetal flow. The centripetal flow is maximum near the membrane and decreases towards the cell's center, in agreement with the experimentally-observed dynamics of the actin network in stationary cells[8]. The cell area at the steady state is smaller than the cell area at the initial time, which implies that contractile forces are greater than protrusive forces. As the cell area decreases, the area constraint ($\boldsymbol{F}_{\text{vol}}$) increases until protrusion, contraction, and area constraint balance at $t \sim 70$ s, when the cell acquires a steady area. To explain the reason the cell does not break symmetry, we computed ρ_Γ and ρ_{cyt} at an arbitrary point of the membrane, which we denote as ρ_Γ^E and ρ_{cyt}^E, respectively. In Fig. 3c, we plotted the time evolution of ρ_Γ^E and ρ_{cyt}^E and we also indicated the values $\rho_{\text{cyt}}^{\text{I}}$ and $\rho_{\text{cyt}}^{\text{II}}$ with green dash-dotted lines. $\rho_{\text{cyt}}^{\text{I}}$ and $\rho_{\text{cyt}}^{\text{II}}$ represent the boundaries between regions I and II, and II and III, respectively, in the f_ρ diagram; see Fig. 2. The pair $(\rho_\Gamma^E, \rho_{\text{cyt}}^E)$ is located very close to the stability line of low ρ_Γ density in region II. Note that $(\rho_\Gamma^E, \rho_{\text{cyt}}^E)$ is located close to, but not exactly on the ρ_Γ stability line because diffusion affects the dynamics of RhoA proteins; see Eqs. (2) and (3). Hereinafter, for the sake of simplicity, we will loosely refer to cases like this as being located on the stability line, although this is only true in an approximate way. The attainment of RhoA bistability requires that, at some region of the membrane, the pair $(\rho_\Gamma^E, \rho_{\text{cyt}}^E)$ transitions to the stability line of high ρ_Γ density. To do so, some stimulus must induce the displacement of $(\rho_\Gamma^E, \rho_{\text{cyt}}^E)$ towards region III in the f_ρ diagram, i.e., must increase ρ_{cyt}^E such that $\rho_{\text{cyt}}^E > \rho_{\text{cyt}}^{\text{II}}$. In conclusion, the cell does not achieve RhoA bistability and, hence, polarization, because (i) the non-polarized initial conditions constitute a quasi-steady state and (ii) the cell does not experience any stimulus strong enough to trigger RhoA bistability. In real cells, spontaneous cell polarization may be caused by random fluctuations of the actin network flow[21]. We cannot reproduce spontaneous cell polarization because we have not included those fluctuations into our model.

4.1.2 Polarized initial conditions

We study three cells with different polarized (i.e., non circularly-symmetric) initial conditions. For each cell, we consider an initially polarized distribution of one of the unknowns ρ_Γ, ρ_{cyt}, or ρ_m, while the other unknowns exhibit a non-polarized (i.e., circularly symmetric) distribution. The parameter values that differ from those given in Section 3.2 are: $\rho_\Gamma^- = 1.22 \mu\text{m}^{-2}$, $\rho_\Gamma^+ = 0.22 \mu\text{m}^{-2}$, and $\rho_{\text{cyt}}^- = \rho_{\text{cyt}}^+ = 1.87 \mu\text{m}^{-2}$ for the ρ_Γ-polarized initial condition (case A1); $\rho_{\text{cyt}}^- = 3.994 \mu\text{m}^{-2}$ and $\rho_{\text{cyt}}^+ = 0 \mu\text{m}^{-2}$ for the ρ_{cyt}-polarized initial condition (case A2); and $\rho_m^- = 0.6 \mu\text{m}^{-2}$ and $\rho_m^+ = 0 \mu\text{m}^{-2}$ for the ρ_m-polarized initial condition (case A3).

Let us focus first on case A1, whose simulation results are plotted in Fig. 4 (the layout is similar to Fig. 3). In Fig. 4a we took advantage of the axis of symmetry traced by the mass center of the cell to plot the ρ_{cyt} distribution on the top half of the cell and the ρ_m and $\boldsymbol{u}$ distributions on the bottom half at four different times. The patch of high ρ_Γ density at the cell's rear promotes myosin association, producing a polarized distribution of myosin (see, e.g., $t = 35$ s). High ρ_m density at the cell's back induces contraction, while low ρ_m density at the cell's front favors protrusion. This polarized state (contraction at the back and protrusion at the front) drives cell motion. Note that, although the ρ_{cyt} dynamics is dominated by diffusion, the ρ_{cyt} distribution is not uniform throughout the cytosol. The cell area at the steady state is larger

---

¶ By isolated environment we refer to an environment in which the cell is not subjected to external stimuli (such as chemical or mechanical stimuli).

‖ The region of low ρ_m density is barely visible due to the color scale of the plot.

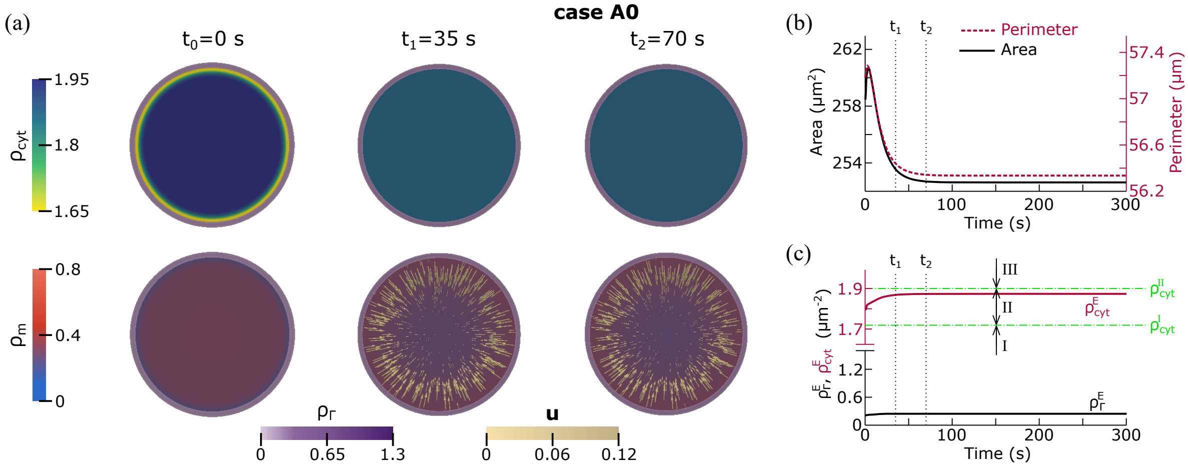

Fig. 3 Non-polarized initial conditions, case A0. *(a)* ρ_Γ and ρ_{cyt} distributions (top row) and ρ_Γ and ρ_m distributions (bottom row) at times $t_0 = 0$, $t_1 = 35$, and $t_2 = 70\,\text{s}$. Arrows in the bottom row represent the velocity $\boldsymbol{u}$. *(b)* Time evolution of the cell area (black solid line) and perimeter (red dashed line). *(c)* Time evolution of ρ_Γ and ρ_{cyt} at the cell's membrane, denoted as ρ^E_Γ (black line) and ρ^E_{cyt} (red line), respectively. The green dash-dotted horizontal lines represent the densities ρ^{I}_{cyt} and ρ^{II}_{cyt}, which separate, respectively, regions I and II, and II and III in the f_ρ diagram (see Fig. 2). Dotted vertical lines in (b) and (c) indicate the times t_1 and t_2.

than the cell area at the initial time; see Fig. 4b. This implies that, in contrast with case A0, the protrusive forces in case A1 are greater than the contractile forces. The mismatch between protrusion and contraction is balanced with the cell area constraint. In Fig. 4c, we plotted the time evolution of the velocity of the cell's center of mass, denoted as u_{cell}. All these results show that a cell with a ρ_Γ-polarized initial condition can initiate motion and achieve a steady motile state. We compute ρ_Γ and ρ_{cyt} at the front and back edges of the cell (over the axis of symmetry) to study RhoA bistability. We denote ρ_Γ and ρ_{cyt} at the front and rear, respectively, as ρ^F_Γ, ρ^F_{cyt}, ρ^R_Γ, and ρ^R_{cyt}. In Fig. 4d we plotted the time evolution of ρ^F_Γ, ρ^R_Γ, ρ^F_{cyt}, and ρ^R_{cyt}. As in Fig. 3c, the green dash-dotted horizontal lines represent the densities ρ^{I}_{cyt} and ρ^{II}_{cyt}, which separate regions I and II, and II and III, respectively, in the f_ρ diagram; see Fig. 2. The pair $(\rho^F_\Gamma, \rho^F_{cyt})$ moves along the stability line of low ρ_Γ density in the f_ρ diagram, while $(\rho^R_\Gamma, \rho^R_{cyt})$ is located on the stability line of high ρ_Γ density. Therefore, the initial conditions represent a bistable state of RhoA proteins, which is maintained during the entire simulation. To gain more insight into the polarization process, we compute the shape factor of the cell (SF) and two polarization factors (P_Γ and P_m, defined below). We define the shape factor as $SF = 4\pi A/p^2$, where A is the cell area and p is the cell perimeter. The shape factor is 1 for a circular cell and decreases as the cell acquires a more canoe-like shape, characteristic of motile keratocytes. The polarization factors quantitatively measure the level of polarization of a system. Different polarization factors have been used in the field of cell migration[33,74]. Here, we propose the polarization factors P_Γ and P_m to study the influence of RhoA proteins and myosin in the polarization of the cell. P_Γ and P_m are associated with ρ_Γ and ρ_m, respectively, and are defined as

$$P_i = \frac{\int_\Omega \delta_\phi \rho_i (x_{\text{cell}} - x)\, \mathrm{d}\Omega}{\int_\Omega \delta_\phi \rho_i |x_{\text{cell}} - x|\, \mathrm{d}\Omega}, \tag{14}$$

where the index i stands for Γ and m, δ_ϕ is the membrane marker defined in Section 2.1, Ω denotes the computational domain, and x_{cell} is the x-coordinate of the mass center of the cell. In our problem, P_i ranges from 0 to 1, where $P_i = 0$ represents a non-polarized state[**] and $P_i = 1$ represents a polarized state with null ρ_i density at the front half of the cell (i.e., ρ_i accumulates only in the back half of the cell). We plotted the time evolution of SF, P_Γ, and P_m in Fig. 4e. According to the initial conditions, $SF = 0$, $0 < P_\Gamma < 1$, and $P_m = 0$ at $t = 0\,\text{s}$. Note that $P_\Gamma < 1$ at $t = 0\,\text{s}$ because $\rho^+_\Gamma = 0.22\,\mu\text{m}^{-2} > 0$. The shape factor decreases and P_m increases as the cell polarizes. The evolution of P_Γ and P_m captures the behavior explained above: The initial conditions represent a polarized (bistable) state of RhoA, very similar to the steady motile state (P_Γ barely changes during the simulation). The polarized state of RhoA proteins induces the polarization of myosin (i.e., the increase of P_m), which drives cell motion. Note that the time evolution of u_{cell} is not related to P_Γ, but analogous to P_m and inversely proportional to SF, which confirms the interplay between cell velocity, cell shape, and cell polarization observed in different works[8,24].

Cases A2 and A3 also attain a polarized and motile steady state. The simulation results of cases A2 and A3 are plotted in Figs. S1 and S2, respectively, in ESI†. The steady states of cases A1, A2, and A3 are identical because N_ρ and N_m take the same values for the three cases. Cases A2 and A3 display slight differences with respect to case A1. In case A2 (ρ_{cyt}-polarized initial conditions), the pair $(\rho^F_\Gamma, \rho^F_{cyt})$ is located on the stability line of low ρ_Γ in the f_ρ diagram. $(\rho^R_\Gamma, \rho^R_{cyt})$ is initially located in region III in the f_ρ diagram, but far from the stability line of high ρ_Γ. The pair $(\rho^R_\Gamma, \rho^R_{cyt})$ quickly moves to the stability line of high ρ_Γ and remains on that stability line for the rest of the simulation. The quick attainment of RhoA bistability is captured by the evolution of P_Γ, which increases from $P_\Gamma = 0$ to $P_\Gamma \approx 0.75$ in less than 5 s; see Fig. S1f.

[**] A non-polarized state corresponds to any ρ_i distribution symmetric with respect to the y-axis at the cell's center of mass, not only to uniform ρ_i distributions.

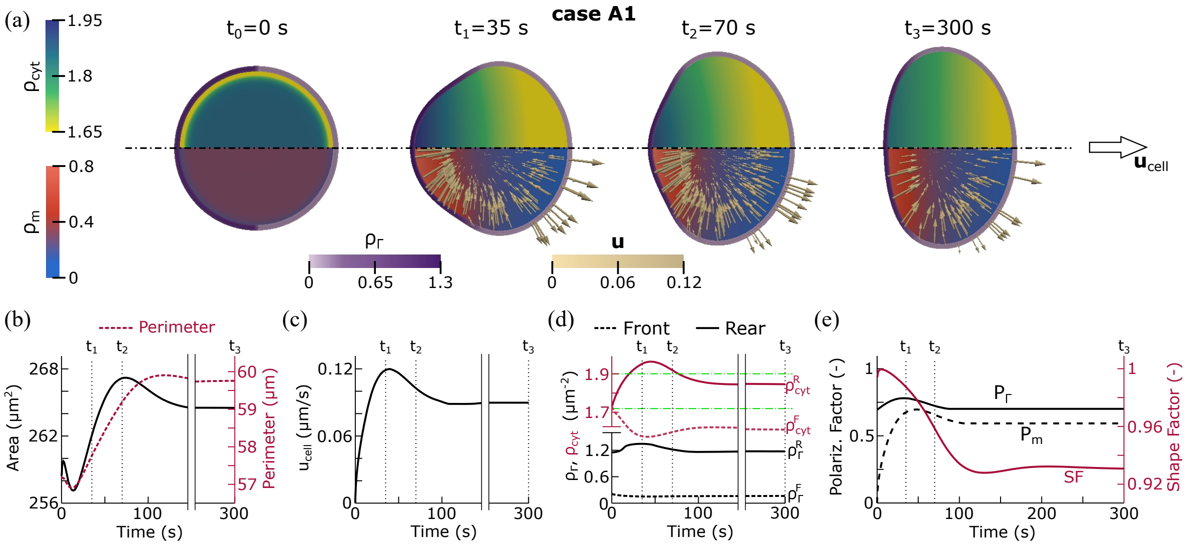

Fig. 4 Polarized initial conditions, case A1. *(a)* ρ_Γ distribution on the membrane and ρ_{cyt} (top half of the cell) and ρ_m (bottom half of the cell) distributions at times 0, 35, 70, and 300s. Arrows in the bottom half of the cell represent the velocity $\boldsymbol{u}$. The cell moves towards the right with its center of mass tracing an axis of symmetry (dash-dotted line). Time evolution of *(b)* the cell area (black solid line) and perimeter (red dashed line); *(c)* the velocity of the cell's center of mass (u_{cell}); *(d)* ρ_Γ (black lines) and ρ_{cyt} (red lines) at the front (dashed lines) and rear (solid lines) edges of the cell on the axis of symmetry, denoted as ρ_Γ^F, ρ_{cyt}^F, ρ_Γ^R, and ρ_{cyt}^R, where the indices F and R stand for front and rear, respectively; and *(e)* cellular shape factor (SF, red solid line) and the polarization factors P_Γ (black solid line) and P_m (black dashed line). The definition of SF, P_Γ, and P_m may be found in Section 4.1.2. The green dash-dotted lines in (d) represent the densities $\rho_{\text{cyt}}^{\text{I}}$ and $\rho_{\text{cyt}}^{\text{II}}$.

Once RhoA proteins display a bistable state, the cell evolves as we described above for case A1. In case A3 (ρ_m-polarized initial conditions), the pair $(\rho_\Gamma^R, \rho_{\text{cyt}}^R)$ is initially located on the stability line of low ρ_Γ in region II; see Fig. S2d. The initially polarized distribution of myosin ($P_m = 1$ at $t = 0\,$s) produces a sudden contraction of the cell's rear, which leads to an increase of ρ_{cyt} in the cell's rear. Hence, ρ_{cyt}^R increases and $(\rho_\Gamma^R, \rho_{\text{cyt}}^R)$ transitions to region III in the f_ρ diagram, where there is a unique stability line corresponding to high ρ_Γ. Therefore, in case A3 the polarization of RhoA is caused by *changes in the cell geometry* driven by the polarized distribution of myosin. The trends of u_{cell} and P_m are analogous, both in cases A2 and A3, which further confirms that u_{cell} is controlled by P_m rather than by P_Γ. From cases A1, A2, and A3 we conclude that P_Γ controls the evolution of P_m because ρ_Γ promotes myosin association, but P_m also controls the evolution of P_Γ by means of the cell geometry. Thus, there is a complex interplay between RhoA proteins, myosin, cell geometry, and cell polarization.

In cases A1, A2, and A3 we considered a steep function as initial distribution of the polarized unknown. We also ran simulations in which we considered a linear function in the x-direction, instead of a steep function, as the initial distribution of the polarized unknown. The simulation results show that the attainment of a polarized and motile steady state depends on the level of polarization given by the initial conditions (data not shown). While a cell with a mildly ρ_Γ-polarized initial condition is able to polarize and move, a cell with a mildly ρ_{cyt}- or ρ_m-polarized initial condition cannot achieve a polarized and motile steady state††.

In conclusion, cell polarization and motion initiation in isolated environments requires initial conditions with a minimum level of polarization.

4.1.3 Limitations to reproduce diverse cell morphodynamics

The model proposed in this paper proves useful to study RhoA-driven cell polarization. However, the analysis of cell morphodynamics using this model displays several drawbacks compared with earlier models proposed by other authors[35,75] and ourselves[54]. On the one hand, we have simplified the dynamics of the adhesion proteins and the actin compounds, which limits the capabilities of the model. On the other hand, the model results are robust to changes in the model parameters. That is, changes in the parameter values do not produce noticeable changes in the steady state of the motile cell. We performed several simulations with different values of N_ρ, $\overline{\eta}_{\text{myo}}$, $\overline{\eta}_{\text{prot}}$, and ρ_m^{prot}. While u_{cell} displays notable differences, the cell shape, area, and the distribution of ρ_{cyt}, ρ_m, and $\boldsymbol{u}$ are similar (compare, e.g., Figs. 4 and 6, where $\overline{\eta}_{\text{myo}} = 60$ and $120\,\text{pN}\mu\text{m}$, respectively). For instance, in Fig. S3 we show the simulation results of a cell with a ρ_Γ-polarized initial condition (case A4), but lower amount of RhoA proteins compared to case A1. The parameters that define the initial conditions take the values $\rho_\Gamma^- = 1.22\mu\text{m}^{-2}$, $\rho_\Gamma^+ = 0.22\mu\text{m}^{-2}$, $\rho_{\text{cyt}}^- = \rho_{\text{cyt}}^+ = 1.75\mu\text{m}^{-2}$, and $\rho_m^- = \rho_m^+ = 0.3\mu\text{m}^{-2}$. Thus, $N_\rho = 460.35$ in case A4, while $N_\rho = 488.9$ for the rest of the cases shown in the paper. The results of case A4 are analogous to those of case A1. Only the cell velocity u_{cell} and the cell shape exhibit some differences: case A4 displays lower u_{cell} and a slightly greater canoe-like shape (compare Figs. 4 and S3).

---

†† According to the notation used in Section 3.2, by mildly ρ_i-polarized initial condition we refer to a initial ρ_i distribution such that $\rho_i(\boldsymbol{x},0) = \delta_{\Omega 0}(\boldsymbol{x})\overline{\rho}_i[1-(x-x_c)/R_c]$, where $\overline{\rho}_i$ is a constant, $\delta_{\Omega 0}(\boldsymbol{x}) = \delta_{\phi 0}(\boldsymbol{x})$ for $\rho_i = \rho_\Gamma$, and $\delta_{\Omega 0}(\boldsymbol{x}) = \phi_0^2(\boldsymbol{x})$ for $\rho_i = \rho_{\text{cyt}}$ and ρ_m.

4.2 Cell polarization depends on the level of myosin activity

Several authors conducted experiments to study the influence of myosin activity on cell polarization. For instance, Verkhovsky and collaborators observed keratocyte polarization in cells with inhibited myosin activity[13]. Yam and collaborators, however, observed that keratocytes require myosin-induced contraction to break the symmetry[20]. They also observed that upregulation of myosin activity does not affect cell polarization. Cells with upregulated myosin activity only exhibit slight changes in their shape and velocity[20]. In this section, we aim at studying the polarization of cells with different levels of myosin activity. To do that, we ran simulations with different values of $\overline{\eta}_{\text{myo}}$, which controls the strength of the contractile forces. From the data given in refs.[13,20], we cannot relate the strength of myosin down- and upregulation with the parameter $\overline{\eta}_{\text{myo}}$. Thus, we opted for taking several values of $\overline{\eta}_{\text{myo}}$. In particular, we took $\overline{\eta}_{\text{myo}} = 12$ (case B1) and 30 pNμm (case B2) to study myosin downregulation, and $\overline{\eta}_{\text{myo}} = 120$ (case B3) and 300 pNμm (case B4) to study myosin upregulation. In our model, the standard value of myosin activity is $\overline{\eta}_{\text{myo}} = 60\,\text{pN}\mu\text{m}$. In Section 4.1.1, we showed that our model requires a polarized initial condition to reproduce cell polarization because the actin flow lacks stochastic fluctuations. To study the influence of $\overline{\eta}_{\text{myo}}$ in the mechanisms of polarization, we must provide an initial condition that permits cell polarization. In cases B1–B4, we considered the ρ_Γ-polarized initial conditions used in case A1; see Fig. 4 and Section 4.1.2. We analyze the simulation results of cases B1–B4 in the following paragraphs.

We plotted the simulation results of case B1 in Fig. 5 with a layout analogous to Fig. 4 (see also Video B1 in ESI†). The time evolution of the cell area and perimeter may be found in Fig. S4. The plot shows that the cell polarizes and moves for $t < 35\,\text{s}$; see u_{cell} in Fig. 5b and P_Γ and P_m in Fig. 5d. Afterwards, u_{cell}, P_Γ, and P_m begin to decrease until the cell achieves a stationary ($u_{\text{cell}} \approx 0$) and non-polarized ($P_\Gamma \approx 0$, $P_m \approx 0$) state at $t \approx 200\,\text{s}$. The loss of polarity is caused by the decrease of myosin-induced contractile strength and can be explained through the following feedback loop: Cell area increases as myosin contraction decreases. Since ρ_{cyt} spreads over a larger area, the total amount of RhoA in the cytosolic form increases. This ρ_{cyt} increase results from membrane-bound ρ_Γ transforming into ρ_{cyt}, which leads to a smaller patch of high ρ_Γ density at the cell's rear (see $t = 120\,\text{s}$ in Fig. 5a). As the patch of high ρ_Γ gets smaller, the amount of associated myosin decreases, which favors protrusion and reduces contraction. This feedback loop ends when the cell area constraint ($\boldsymbol{F}_{\text{vol}}$) balances the protrusive and contractile forces. In case B1, equilibrium is achieved when the patch of high ρ_Γ density has vanished and, hence, cell polarity has been lost. Cells with levels of myosin inhibition lower than case B1 (e.g., case B2) achieve equilibrium before the patch of high ρ_Γ vanishes, which implies that cell polarity is maintained (see case B2 in Fig. S4). Different plots in Fig. 5 capture the effects of this feedback loop. As associated myosin decreases at the cell's back, the cell cannot retract its rear and u_{cell} decreases; see Fig. 5b. The pair $(\rho_\Gamma^F, \rho_{\text{cyt}}^F)$ is located on the stability line of low ρ_Γ density in the f_ρ diagram for all t; see Fig. 5c. The pair $(\rho_\Gamma^R, \rho_{\text{cyt}}^R)$ is initially located on the stability line of high ρ_Γ in region II. As the patch of high ρ_Γ density on the membrane becomes smaller, both ρ_Γ^R and ρ_{cyt}^R decrease (see the time interval $70\,\text{s} < t < 120\,\text{s}$ in Fig. 5c). At $t \approx 150\,\text{s}$, the patch of high ρ_Γ density vanishes, i.e., $(\rho_\Gamma^R, \rho_{\text{cyt}}^R)$ moves to the stability line of low ρ_Γ in region II. Note that the transition of $(\rho_\Gamma^R, \rho_{\text{cyt}}^R)$ from the high to the low ρ_Γ stability line occurs in region II and not in region I (i.e., $\rho_{\text{cyt}}^R > \rho_{\text{cyt}}^{\text{I}}$ when ρ_Γ^R takes the low stable density). This indicates that geometry constraints and diffusion are dominating the dynamics of RhoA, rather than the reaction term f_ρ; see Eqs. (2) and (3). In Fig. 5d, P_Γ and P_m further confirm the gradual loss of polarity of RhoA proteins and myosin, respectively. P_Γ approaches 0 when the patch of high ρ_Γ at the cell's rear vanishes ($t \approx 150\,\text{s}$). P_m approaches 0 at $t \approx 200\,\text{s}$, later than P_Γ, which suggests that myosin dynamics is slower than RhoA dynamics. *SF* decreases until $t \approx 150\,\text{s}$ and increases afterwards; see Fig. 5d. At $t \approx 300\,\text{s}$ the cell does not display a circular geometry yet. These results indicate that the loss of polarity displayed by the cell geometry is much slower than the loss of polarity of myosin or RhoA proteins.

The results show that cells with low levels of myosin inhibition attain a polarized and motile steady state (see, e.g., case B2 in Fig. S4). In case B2, the cell achieves equilibrium before the patch of high ρ_Γ at the cell's rear vanishes (see Video B2 in ESI†). Compared to case A1, in case B2 the patch of high ρ_Γ is smaller and the cell's rear retracts more slowly, which leads to a lower cell velocity u_{cell}.

Case B3 represents a cell with a low level of myosin upregulation. We plotted the simulation results in Fig. 6. The cell achieves a polarized and motile steady state, in which the cell area is smaller than in case A1 (cell with standard myosin activity). Cells with myosin upregulation exhibit the opposite feedback loop that cells with myosin downregulation. For myosin-upregulated cells, large myosin contraction leads to smaller cells, so that the patch of high ρ_Γ at the cell's rear grows and the amount of associated myosin increases; see Fig. 6a. More associated myosin implies that (i) u_{cell} increases because the cell's rear retracts faster and (ii) the retrograde flow $\boldsymbol{u}$ increases (not shown in Fig. 6a), which leads to a steeper distribution of ρ_m, i.e., a more polarized ρ_m distribution. The polarization factor P_m confirms point (ii): P_m in the steady state of case B3 ($P_m \approx 0.75$, see Fig. 6d) is larger than in case A1 ($P_m \approx 0.6$, see Fig. 4e). The pair $(\rho_\Gamma^F, \rho_{\text{cyt}}^F)$ is located on the stability line of low ρ_Γ in region I (see Fig. 6b), while $(\rho_\Gamma^R, \rho_{\text{cyt}}^R)$ is on the stability line of high ρ_Γ in region III (see Fig. 6c). The fact that $(\rho_\Gamma^F, \rho_{\text{cyt}}^F)$ is located in region I and $(\rho_\Gamma^R, \rho_{\text{cyt}}^R)$ in region III, far from the transitions between region II and III and region I and II, respectively, indicates that myosin upregulation enhances RhoA bistability and, hence, cell polarity. High levels of myosin upregulation (e.g., case B4) produce huge contractile forces. Protrusion and the cell area constraint cannot balance contraction and the cell shrinks and eventually disappears (results not shown).

In conclusion, our results do not contradict ref.[13] and ref.[20] because we cannot relate the experimental level of myosin inhibition with the model parameter $\overline{\eta}_{\text{myo}}$. Our results show that cells polarize or not depending on the level of myosin downregulation. We hypothesize that the discrepancy between ref.[13] and ref.[20] is due to the application of different levels of myosin inhi-

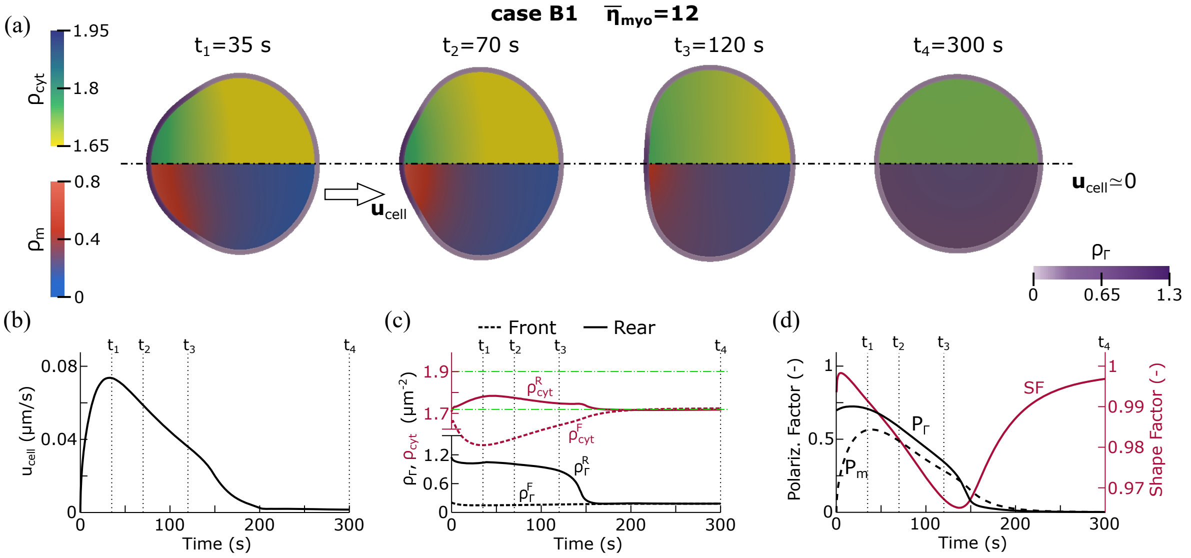

Fig. 5 Downregulation of myosin activity, case B1 ($\overline{\eta}_{\text{myo}} = 12\,\text{pN}\mu\text{m}$). The layout of the figure is analogous to Fig. 4. *(a)* ρ_Γ, ρ_{cyt} (top half of the cell), and ρ_m (bottom half of the cell) distributions at times 35, 70, 120, and 300s. The initial conditions are the same as shown in Fig. 4. Time evolution of *(b)* cell's velocity u_{cell}; *(c)* ρ_Γ (black lines) and ρ_{cyt} (red lines) at the front (F, dashed lines) and rear (R, solid lines) edges of the cell at the axis of symmetry, denoted as ρ^F_Γ, ρ^F_{cyt}, ρ^R_Γ, and ρ^R_{cyt}, respectively; and *(d)* cellular shape factor (SF, red solid line) and the polarization factors P_Γ (black solid line) and P_m (black dashed line). The green dash-dotted lines in (c) represent the densities $\rho^{\text{I}}_{\text{cyt}}$ and $\rho^{\text{II}}_{\text{cyt}}$.

bition in their experiments. In addition, our results confirm that myosin upregulation does not impede cell polarization, as stated by ref.[20]. In fact, myosin upregulation favors cell polarization.

4.3 Spatially-localized variations of myosin activity trigger cell polarization

Yam and collaborators studied in detail the influence of myosin activity in cell polarization[20]. One of the experimental setups consisted of down- and up-regulating myosin activity at some regions of stationary keratocytes. The results of this experiment are surprising. Whereas spatially-localized myosin upregulation leads to cell polarization, spatially-localized myosin inhibition does not induce cell polarization. Our goal in this section is to shed light into the mechanisms of cell polarization when a stationary cell is subjected to spatially-localized variations of myosin activity. Thus, we run simulations in which we try to replicate the experiments performed in ref.[20]. In those experiments, the drugs (*blebbistain* for myosin inhibition and *calyculin A* for myosin overactivation) are applied through a micropipette located near the cell's boundary. The micropipette moves according to the motion of the cell's boundary. The treatment ceases when the cell moves $\sim 1/2$ of its radius. Instead of incorporating a PDE to account for the diffusion of the drug, we opted for simplifying the drug's dynamics. We assumed that the drug equally affects half a cell for a time interval t_{myo}. After t_{myo}, the effect of the drug vanishes. Mathematically, we spatially and temporarily modify the myosin-induced contractile stress such that

$$\overline{\eta}_{\text{myo}} = \begin{cases} \overline{\eta}^i_{\text{myo}} & \text{if } \boldsymbol{x} \in \Omega_M \text{ and } t < t_{\text{myo}}, \\ 60\,\text{pN}\mu\text{m} & \text{otherwise}, \end{cases} \tag{15}$$

where $\overline{\eta}^i_{\text{myo}}$ is the down- or up-regulated value of $\overline{\eta}_{\text{myo}}$ and Ω_M denotes the half of the cell where down- or up-regulation occurs. If $\overline{\eta}^i_{\text{myo}} < 60\,\text{pN}\mu\text{m}$ (myosin inhibition), we consider $\Omega_M = \{\boldsymbol{x} : x > x_{\text{cell}}\}$ where x_{cell} is the x-coordinate of the cell's center of mass. If $\overline{\eta}^i_{\text{myo}} > 60\,\text{pN}\mu\text{m}$ (myosin upregulation), we consider $\Omega_M = \{\boldsymbol{x} : x < x_{\text{cell}}\}$. We propose a dual definition for Ω_M so that the cell, if initiates motion, moves to the right for both down- and up-regulation of myosin activity. We take $t_{\text{myo}} = 40\,\text{s}$ and consider a non-polarized (and stationary) cell as initial conditions, with the parameter values given in Section 3.2. A plot with the non-polarized initial conditions may be found in Fig. 3a. Since we cannot relate the level of myosin inhibition or upregulation with $\overline{\eta}^i_{\text{myo}}$, we run simulations with different values of $\overline{\eta}^i_{\text{myo}}$. We take $\overline{\eta}^i_{\text{myo}} = 12$ (case C1), 30 (case C2), and $45\,\text{pN}\mu\text{m}$ (case C3) for spatially-localized myosin downregulation, and $\overline{\eta}^i_{\text{myo}} = 80$ (case C4), 120 (case C5), and $300\,\text{pN}\mu\text{m}$ (case C6) for upregulation.

Cells with high levels of spatially-localized myosin inhibition (cases C1 and C2) achieve a polarized and motile steady state. We plotted the simulation results of case C2 in Fig. 7 (see also Video C2 in ESI†). The striped region in Fig. 7a represents the half of the cell where myosin activity is downregulated. Due to myosin inhibition, protrusion is larger than contraction at the cell's front, which induces the forward movement of the membrane. However, the cell's back barely retracts during the first seconds ($t < 5\,\text{s}$) because protrusion and contraction are balanced. Myosin diffusion cannot balance the membrane's deformation at the cell's front so that ρ_m acquires a non-uniform distribution. The asymmetric ρ_m distribution along the x-axis generates retrograde actin flow, which increases the asymmetry of the ρ_m distribution. Thus, myosin gradually accumulates at the cell's back and promotes the retraction of the membrane. At $t \approx 10\,\text{s}$, the membrane at the front and rear of the cell moves at the same velocity (data not shown).

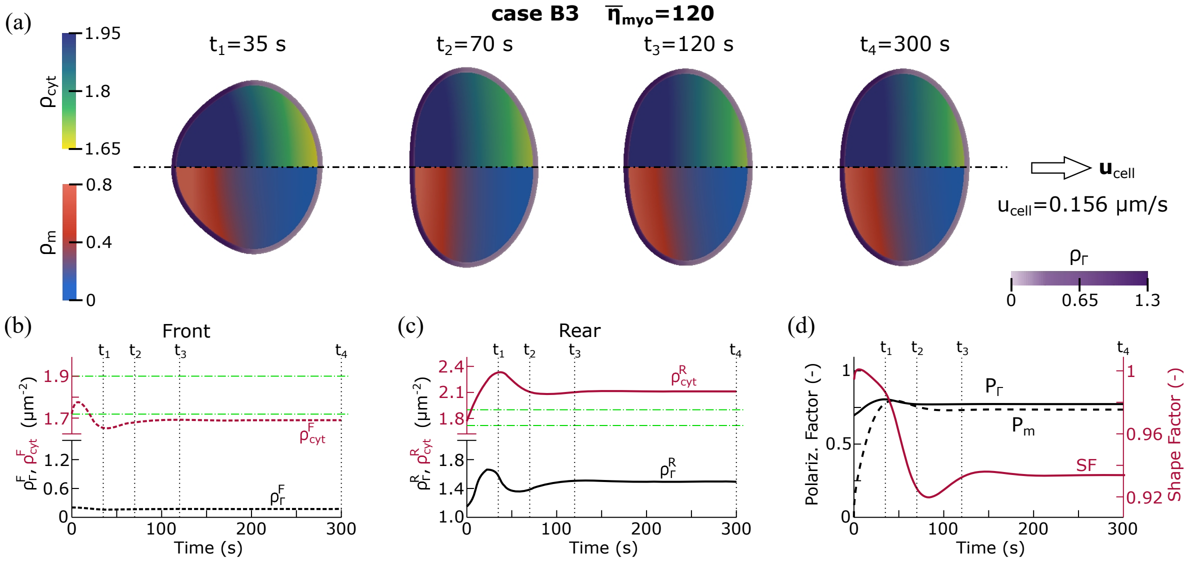

Fig. 6 Upregulation of myosin activity, case B3 ($\overline{\eta}_{\text{myo}} = 120\,\text{pN}\mu\text{m}$). The layout of the figure is analogous to Fig. 5. *(a)* ρ_Γ, ρ_{cyt} (top half of the cell), and ρ_m (bottom half of the cell) distributions at times 35, 70, 120, and 300 s. The initial conditions are the same as shown in Fig. 4. Time evolution of *(b)* ρ_Γ (black line) and ρ_{cyt} (red line) at the front edge of the cell on the axis of symmetry; *(c)* ρ_Γ (black line) and ρ_{cyt} (red line) at the rear edge of the cell on the axis of symmetry; and *(d)* cellular shape factor (SF, red solid line) and the polarization factors P_Γ (black solid line) and P_m (black dashed line). The green dash-dotted lines in (b) and (c) represent the densities $\rho_{\text{cyt}}^{\text{I}}$ and $\rho_{\text{cyt}}^{\text{II}}$.

For $t > 10\,\text{s}$, the cell velocity keeps increasing (see Fig. 7b) and ρ_m and ρ_{cyt} continue to accumulate at the cell's rear until $t = t_{\text{myo}}$ (see P_Γ and P_m in Fig. 7d). At $t = t_{\text{myo}}$, myosin inhibition ceases and $\overline{\eta}_{\text{myo}}$ suddenly changes from 30 to $60\,\text{pN}\mu\text{m}$ in the front half of the cell. This sudden change of $\overline{\eta}_{\text{myo}}$ explains the sharp transition of u_{cell}. RhoA proteins do not display bistability at $t = t_{\text{myo}}$. Both $(\rho_\Gamma^F, \rho_{\text{cyt}}^F)$ and $(\rho_\Gamma^R, \rho_{\text{cyt}}^R)$ are located on the stability line of low ρ_Γ; see Fig. 7c. However, RhoA and myosin distributions are slightly polarized ($P_\Gamma > 0$ and $P_m > 0$ at $t = t_{\text{myo}}$; see Fig. 7d). The level of polarization does not decrease after $t = t_{\text{myo}}$. In fact, ρ_{cyt}^R gradually increases until $\rho_{\text{cyt}}^R > \rho_{\text{cyt}}^{\text{II}}$ at $t \approx 75\,\text{s}$. At that time, the pair $(\rho_\Gamma^R, \rho_{\text{cyt}}^R)$ enters in region III in the f_ρ diagram and transitions to the stability line of high ρ_Γ. RhoA bistability is achieved and the cell quickly polarizes, increases its velocity, and attains a motile steady state; see u_{cell}, P_Γ, and P_m after $t \approx 75\,\text{s}$. At this point, we want to remark two ideas. First, although the ρ_Γ and ρ_m distributions are slightly polarized at $t = t_{\text{myo}}$, the geometry of the cell is essentially circular. SF begins to decrease when the ρ_Γ and ρ_m distributions are highly polarized. Second, ρ_{cyt}^R exhibits a valley at $t \approx 85\,\text{s}$. At that time, ρ_Γ^R is increasing towards the high ρ_Γ stable density. The ρ_Γ^R increase implies that ρ_{cyt} is transforming into ρ_Γ at the cell's rear. ρ_{cyt}^R temporarily decreases because ρ_{cyt} transformation into ρ_Γ cannot be instantly balanced by ρ_{cyt} diffusion. The pair $(\rho_\Gamma^R, \rho_{\text{cyt}}^R)$ moves back to region II in the f_ρ diagram during the ρ_{cyt}^R trough. However, $(\rho_\Gamma^R, \rho_{\text{cyt}}^R)$ moves back to a region where $f_\rho > 0$ in region II (see Fig. 2), which explains why ρ_Γ^R keeps increasing until ρ_Γ^R reaches the high ρ_Γ stable density.

Low levels of spatially-localized myosin inhibition (e.g., case C3) cannot induce cell polarization and motion. The main results of case C3 may be found in Fig. S5 and Video C3 in ESI†. The behavior of case C3 until $t = t_{\text{myo}}$ is analogous to that of case C2. However, P_Γ and P_m in case C3 are lower at $t = t_{\text{myo}}$ and gradually decrease after $t = t_{\text{myo}}$. At $t = t_{\text{myo}}$, $(\rho_\Gamma^R, \rho_{\text{cyt}}^R)$ is located on the stability line of low ρ_Γ in region II. After $t = t_{\text{myo}}$, ρ_{cyt}^R increases but does not reach $\rho_{\text{cyt}}^{\text{II}}$. Thus, $(\rho_\Gamma^R, \rho_{\text{cyt}}^R)$ does not transition to the stability line of high ρ_Γ and RhoA bistability is not attained.

Low (case C4) and intermediate (case C5) levels of spatially-localized myosin upregulation induce cell polarization and motion. We plotted the simulation results of case C4 and case C5 in Figs. S6 and 8, respectively (see also Video C4 in ESI†). Since the results of both cases are analogous, we focus on case C5. In case of spatially-localized myosin upregulation, the cell's rear moves forward faster than the cell's front during the drug treatment ($t < t_{\text{myo}}$). The velocities of the front and rear edges match 7 s after the treatment ceases. Since the cell's rear retracts faster than in case C2, ρ_{cyt} and ρ_m accumulate more rapidly at the rear, which promotes a faster polarization of the cell (compare P_Γ and P_m in Figs. 7d and 8e). In case C5, due to the quick accumulation of ρ_{cyt} at the cell's rear, the pair $(\rho_\Gamma^R, \rho_{\text{cyt}}^R)$ quickly transitions from region II to region III in the f_ρ diagram. At $t \approx 20\,\text{s}$, $(\rho_\Gamma^R, \rho_{\text{cyt}}^R)$ is located on the stability line of high ρ_Γ and RhoA bistability is attained. Note that the ρ_Γ^R transition from the low to the high stable density originates a trough-like oscillation in ρ_{cyt}^R; see $t \approx 20\,\text{s}$ in Fig. 8d. After the drug is removed at t_{myo}, the cell remains polarized and achieves a steady motile state at $t \approx 120\,\text{s}$. As observed in the previous section, extremely high levels of myosin upregulation (e.g., case C6) produce unrealistic results, in which the cell shrinks and disappears (data not shown).

In conclusion, spatially-localized down- and up-regulation of myosin activity induce cell polarization, except for low levels of downregulation. Therefore, spatially-localized upregulation of myosin activity favors cell polarization in comparison with downregulation, which may explain the experimental observations in ref.[20]. We hypothesize that keratocytes in ref.[20] were exposed to

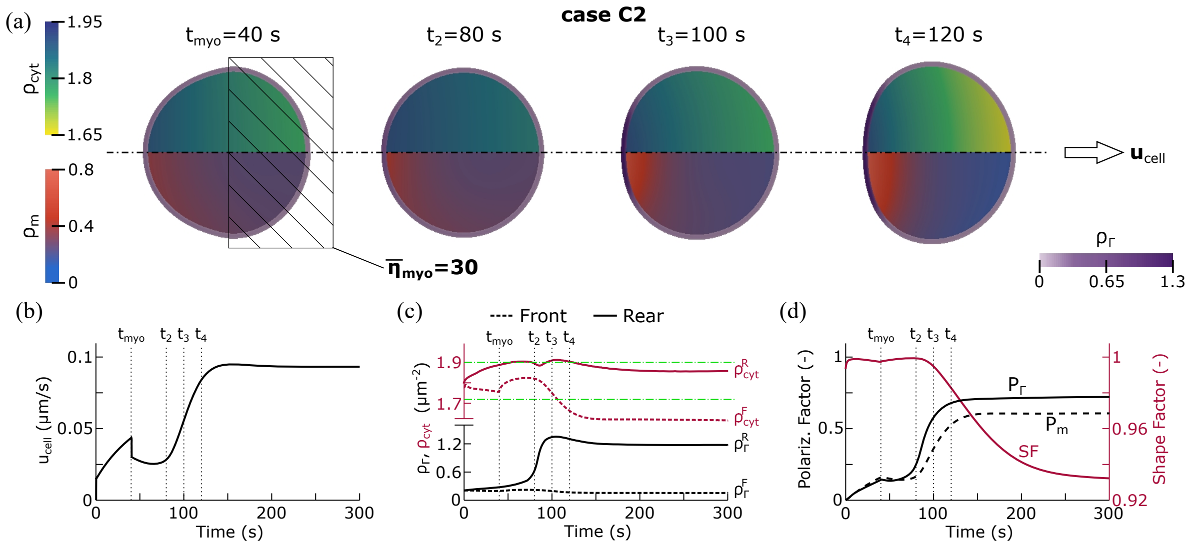

Fig. 7 Spatially-localized downregulation of myosin activity (case C2). Myosin activity is reduced such that $\overline{\eta}_{\text{myo}} = 30\,\text{pN}\mu\text{m}$ in the front half of the cell for $t < t_{\text{myo}} = 40\,\text{s}$. Otherwise, $\overline{\eta}_{\text{myo}} = 60\,\text{pN}\mu\text{m}$. The layout of the figure is analogous to Fig. 5. *(a)* ρ_Γ, ρ_{cyt} (top half of the cell), and ρ_m (bottom half of the cell) distributions at times 40, 80, 100, and 120 s. The initial conditions are the same as shown in Fig. 3. Time evolution of *(b)* u_{cell}; *(c)* ρ^F_Γ (black dashed line), ρ^F_{cyt} (red dashed line), ρ^R_Γ (black solid line), and ρ^R_{cyt} (red solid line); and *(d) SF* (red solid line), P_Γ (black solid line), and P_m (black dashed line). The green dash-dotted lines in (c) represent the densities $\rho^{\text{I}}_{\text{cyt}}$ and $\rho^{\text{II}}_{\text{cyt}}$; see Fig. 2.

low levels of myosin down- and up-regulation. Our results also suggest that the attainment of a steady polarized state depends on the level of polarization displayed by RhoA proteins and myosin, i.e., by P_Γ and P_m, when myosin down- and up-regulation ceases.

4.4 Cell polarization by mechanical impact

In this section we study cell polarization induced by mechanical cues. Verkhovsky and collaborators observed that cell polarization is induced not only by cell-cell collisions, but also by the application of an external pressure on the cell's membrane [13]. In particular, the authors apply a high-pressure flow through a micropipette located near the membrane of a stationary keratocyte [13]. The micropipette moves according to the motion of the adjacent membrane until the membrane deforms $\sim 1/3$ or $1/2$ of the cell's diameter. At that time, the micropipette is removed. Here, our goal is to computationally study that experiment and provide more insight into the mechanisms of cell polarization by mechanical impact. We run a simulation (case D0) in which we model the impact of the high-pressure flow as a circular object pushing the cell's membrane. We consider an object of radius R_{imp}, which moves along the x-axis with constant velocity u_{imp}. The object is removed at time t_{imp}. From ref. [13], we can estimate the values of R_{imp}, u_{imp}, and t_{imp} as $R_{\text{imp}} = 2.25\,\mu\text{m}$, $u_{\text{imp}} = 0.08\,\mu\text{m}\,\text{s}^{-1}$, and $t_{\text{imp}} = 85\,\text{s}$. We consider a stationary non-polarized cell as initial conditions; see $t = 0\,\text{s}$ in Fig. 9a. The parameter values for the initial conditions are those given in Section 3.2. The initial distance between the edges of the cell and the object is $10u_{\text{imp}} + d_{\text{rep}}$; see $t = 0\,\text{s}$ in Fig. 9a. We incorporate that distance so that the object starts pushing the cell (via the force $\nabla \cdot \boldsymbol{\sigma}_{\text{rep}}$) 10 s after the object starts moving. Note that d_{rep} represents the cell-object distance at which $\boldsymbol{\sigma}_{\text{rep}}$ is activated; see Eq. (7). The simulation results of case D0 are plotted in Fig. 9. The cell's rear moves forward due to the application of the pushing force; see Fig. 9a. As the cell's back end retracts, ρ_m and ρ_{cyt} increase at the cell's rear. Thus, ρ^R_{cyt} increases and $(\rho^R_\Gamma, \rho^R_{\text{cyt}})$ quickly transitions from region II to region III in the f_ρ diagram; see ρ^R_{cyt} in Fig. 9c. Once in region III, $(\rho^R_\Gamma, \rho^R_{\text{cyt}})$ moves to the stability line of high ρ_Γ at $t \approx 50\,\text{s}$ and RhoA proteins exhibit a bistable state. RhoA bistability is maintained after the mechanical stimulus vanishes at $t = t_{\text{imp}}$. In Fig. 9d, the evolution of P_Γ and P_m shows that RhoA and myosin completely polarize before $t = t_{\text{imp}}$. The cell reaches a steady motile state at $t \approx 200\,\text{s}$; see *SF* in Fig. 9d.

Case D0 proves that our model can explain cell polarization by mechanical impact, as observed in ref. [13]. We next run different simulations to analyze the influence of the experimental parameters R_{imp}, u_{imp}, and t_{imp}. In those simulations, we consider the same initial conditions as in case D0 and we only change the value of R_{imp}, u_{imp}, or t_{imp}. We first study the influence of R_{imp}. We compare the results of three simulations with $R_{\text{imp}} = 1.5$, 2.25 (case D0), and $3\,\mu\text{m}$ in Fig. S7. The results are almost indistinguishable for the three cases, which indicates that the influence of the pushing object size in cell polarization is insignificant. We next study the influence of u_{imp}. We run simulations with $u_{\text{imp}} = 0.01$, 0.04, 0.08 (case D0), and $0.12\,\mu\text{m}\,\text{s}^{-1}$. We plotted the simulation results in Fig. S8. The cell polarizes and attains a steady motile state for $u_{\text{imp}} = 0.04$, 0.08, and $0.12\,\mu\text{m}\,\text{s}^{-1}$. However, the cell does not polarizes or move for $u_{\text{imp}} = 0.01\,\mu\text{m}\,\text{s}^{-1}$. The case $u_{\text{imp}} = 0\,\mu\text{m}\,\text{s}^{-1}$, in which the object does not move, is equivalent to case A0 (a cell in an isolated environment with non-polarized initial conditions). In case A0, the cell displays a non-polarized and stationary steady state. Therefore, there is a value of u_{imp} that establishes the boundary between attaining cell polarization or not. From our results, the u_{imp} threshold for cell polarization is between $u_{\text{imp}} = 0.01\,\mu\text{m}\,\text{s}^{-1}$ and $u_{\text{imp}} = 0.02\,\mu\text{m}\,\text{s}^{-1}$ (data not shown). As

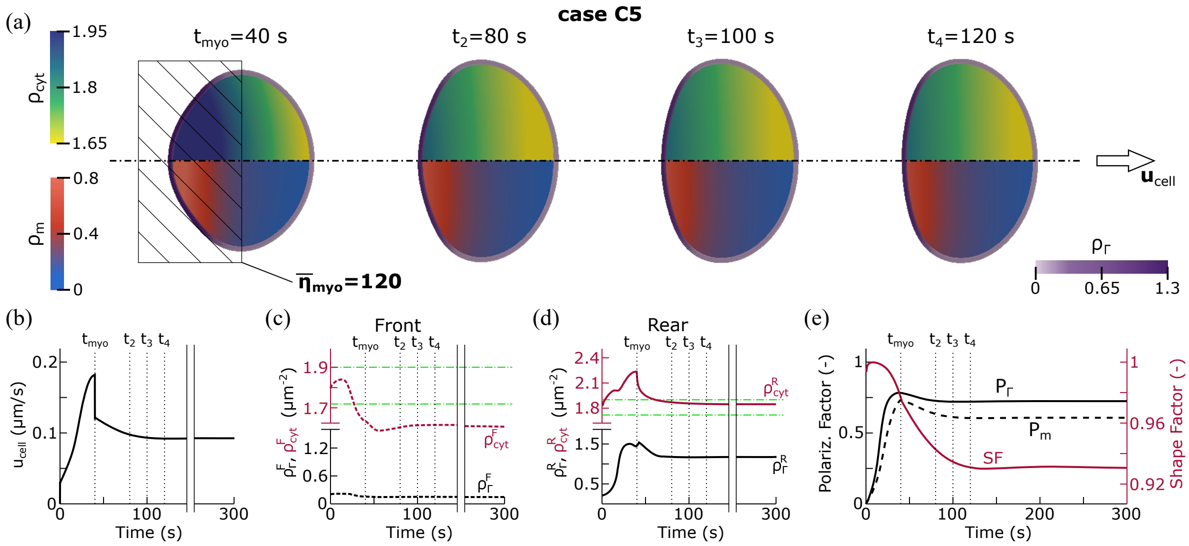

Fig. 8 Spatially-localized upregulation of myosin activity (case C5). Myosin activity is increased such that $\overline{\eta}_{\text{myo}} = 120\,\text{pN}\mu\text{m}$ in the rear half of the cell for $t < t_{\text{myo}} = 40\,\text{s}$. Otherwise, $\overline{\eta}_{\text{myo}} = 60\,\text{pN}\mu\text{m}$. The layout of the figure is analogous to Fig. 7. *(a)* ρ_Γ, ρ_{cyt} (top half of the cell), and ρ_m (bottom half of the cell) distributions at times 40, 80, 100, and 120 s. The initial conditions are the same as shown in Fig. 3. Time evolution of *(b)* u_{cell}; *(c)* ρ_Γ^F (black line) and ρ_{cyt}^F (red line); *(d)* ρ_Γ^R (black line) and ρ_{cyt}^R (red line); and *(e)* SF (red solid line), P_Γ (black solid line), and P_m (black dashed line). The green dash-dotted lines in (c) and (d) represent the densities $\rho_{\text{cyt}}^{\text{I}}$ and $\rho_{\text{cyt}}^{\text{II}}$; see Fig. 2.

u_{imp} increases beyond that threshold, the cell achieves a polarized state faster; see Figs. S8e-f. This is expected because a faster membrane deformation, caused by higher u_{imp}, induces higher ρ_{cyt} density at the cell's rear. The sooner $\rho_{\text{cyt}}^R > \rho_{\text{cyt}}^{\text{II}}$, the sooner RhoA proteins attain bistability and the cell polarizes. We finally study the influence of t_{imp}. We analyze the results of three simulations with $t_{\text{imp}} = 25$, 35, and 85 s (case D0). The simulation results may be found in Fig. S9. For $t_{\text{imp}} = 25\,\text{s}$ the cell does not polarize, whereas for $t_{\text{imp}} = 35\,\text{s}$ the cell does polarize. The results show that there is a t_{imp} threshold for cell polarization and is between $t_{\text{imp}} = 25\,\text{s}$ and $t_{\text{imp}} = 35\,\text{s}$. The time evolution of $(\rho_\Gamma^R, \rho_{\text{cyt}}^R)$ for $t_{\text{imp}} = 25$ and 35 s captures the complex dynamics of RhoA proteins; see Fig. S9c. $(\rho_\Gamma^R, \rho_{\text{cyt}}^R)$ is initially located on the stability line of low ρ_Γ in both cases $t_{\text{imp}} = 25$ and 35 s. Likewise, the pairs $(\rho_\Gamma^R, \rho_{\text{cyt}}^R)$ transition to region III in the f_ρ diagram before the pushing object is removed at $t = t_{\text{imp}}$, i.e., $\rho_{\text{cyt}}^R > \rho_{\text{cyt}}^{\text{II}}$ at $t = t_{\text{imp}}$ in both cases. Upon removing the object, $(\rho_\Gamma^R, \rho_{\text{cyt}}^R)$ quickly returns to region II in the f_ρ diagram, i.e., $\rho_{\text{cyt}}^{\text{I}} < \rho_{\text{cyt}}^R < \rho_{\text{cyt}}^{\text{II}}$ in both cases. In the case $t_{\text{imp}} = 25\,\text{s}$, the pair $(\rho_\Gamma^R, \rho_{\text{cyt}}^R)$ returns to a region in which $f_\rho < 0$, so that ρ_Γ is attracted to the stability line of low ρ_Γ; see Fig. 2. However, in the case $t_{\text{imp}} = 35\,\text{s}$, when $(\rho_\Gamma^R, \rho_{\text{cyt}}^R)$ returns to region II, the high density of ρ_Γ^R provokes that $(\rho_\Gamma^R, \rho_{\text{cyt}}^R)$ is located in the region in which $f_\rho > 0$. This explains why the case $t_{\text{imp}} = 35\,\text{s}$ attains RhoA bistability and the case $t_{\text{imp}} = 25\,\text{s}$ does not. The evolution of P_Γ and P_m further confirms the conclusion stated in the previous section: the attainment of cell polarization depends on the value of the polarization factors when the external stimulus (here, the pushing force) ceases. We discuss this idea in the next paragraph and in Section 5.

Verkhovsky and collaborators observed the initiation of cell motion induced by mechanical impact both in the presence and absence of myosin inhibition[13]. We leverage our model to study the influence of myosin inhibition in cell polarization by mechanical cues. The information provided in ref.[13] about the inhibition of myosin is scarce. We assume that myosin activity is reduced during the mechanical stimulation and recovers its standard value 15 s after the mechanical stimulus vanishes. Thus, the pushing object is removed at $t_{\text{imp}} = 85\,\text{s}$ and myosin inhibition ceases at $t_{\text{myo}} = 100\,\text{s}$. We run two simulations in which we downregulated myosin activity to $\overline{\eta}_{\text{myo}} = 12\,\text{pN}\mu\text{m}$ (case D1) and $\overline{\eta}_{\text{myo}} = 30\,\text{pN}\mu\text{m}$ (case D2) for $t < t_{\text{myo}}$. After $t = t_{\text{myo}}$, the myosin-induced contractile strength recovers its standard value $\overline{\eta}_{\text{myo}} = 60\,\text{pN}\mu\text{m}$. The rest of the parameter values and initial conditions are identical to case D0. We run the simulations of cases D1 and D2 until $t = 600\,\text{s}$, instead of 300 s, so that the cell can achieve a steady state. The simulation results of cases D1 and D2 may be found in Fig. S10 and Videos D1 and D2 in ESI†. In Fig. 10, we compare the time evolution of ρ_Γ^F, ρ_{cyt}^F, ρ_Γ^R, ρ_{cyt}^R, P_Γ, and P_m for cases D0, D1, and D2. Case D2 attains a polarized and motile steady state but case D1 does not. The time case D2 attains RhoA bistability is a surprising result. RhoA bistability is achieved at $t \approx 300\,\text{s}$, i.e., 200 s after the last stimulus ceases. In cases D1 and D2, $(\rho_\Gamma^F, \rho_{\text{cyt}}^F)$ is located on the stability line of low ρ_Γ in the f_ρ diagram; see Fig. 10a. At $t = t_{\text{myo}}$, $(\rho_\Gamma^R, \rho_{\text{cyt}}^R)$ is located on the stability line of low ρ_Γ in both cases D1 and D2; see Fig. 10b. For $t > t_{\text{myo}}$, ρ_Γ^R and ρ_{cyt}^R increase in both cases D1 and D2. However, only in case D2 ρ_{cyt}^R reaches the value $\rho_{\text{cyt}}^{\text{II}}$ (at $t \approx 300\,\text{s}$) and $(\rho_\Gamma^R, \rho_{\text{cyt}}^R)$ transitions to the stability line of high ρ_Γ. In case D1, $(\rho_\Gamma^R, \rho_{\text{cyt}}^R)$ displays a steady state on the stability line of low ρ_Γ and ρ_{cyt}^R never reaches the value $\rho_{\text{cyt}}^{\text{II}}$. The time evolution of P_Γ and P_m allows us to gain insights into the differences between cases D1 and D2. Let us focus first on P_Γ, which is plotted in Fig. 10c. In both cases D1 and D2, P_Γ increases until the mechanical stimulus is removed at $t = t_{\text{imp}}$ and decreases from $t = t_{\text{imp}}$ to $t = t_{\text{myo}}$. Once the chemical stimulus vanishes at $t = t_{\text{myo}}$, P_Γ gradually decreases in case D1 but slightly increases in case D2. The sudden increase of P_Γ at $t \approx 300\,\text{s}$ in case D2 captures

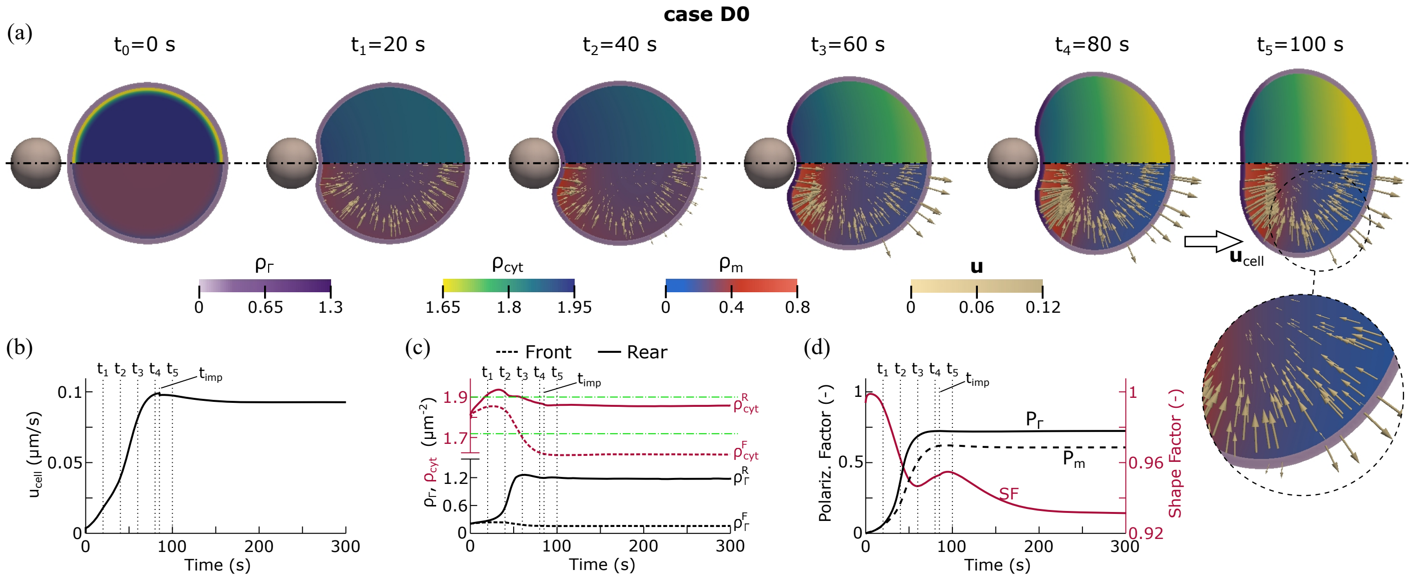

Fig. 9 Cell polarization by mechanical impact, case D0. A circular object moves with constant velocity $u_{\text{imp}} = 0.08\,\mu\text{m}\,\text{s}^{-1}$ along the x-axis pushing the cell. The object is removed at $t_{\text{imp}} = 85\,\text{s}$. The layout of the figure is analogous to the previous figures. *(a)* ρ_Γ, ρ_{cyt} (top half of the cell), and ρ_m (bottom half of the cell) distributions at times 0, 20, 40, 60, 80, and 100 s. Arrows in the bottom half of the cell represent the velocity $\boldsymbol{u}$. Time evolution of *(b)* u_{cell}; *(c)* ρ_Γ^F (black dashed line), ρ_{cyt}^F (red dashed line), ρ_Γ^R (black solid line), and ρ_{cyt}^R (red solid line); and *(d)* SF (red solid line), P_Γ (black solid line), and P_m (black dashed line). The green dash-dotted lines in (c) represent the densities $\rho_{\text{cyt}}^{\text{I}}$ and $\rho_{\text{cyt}}^{\text{II}}$; see Fig. 2.

the attainment of RhoA bistability. P_m, however, decreases both after $t = t_{\text{imp}}$ and $t = t_{\text{myo}}$ in cases D1 and D2; see Fig. 10d. In case D1, P_m monotonically decreases after $t = t_{\text{imp}}$ until the end of the simulation. In case D2, P_m exhibits a plateau for $150\,\text{s} < t < 300\,\text{s}$ and increases after $t \approx 300\,\text{s}$. At the end of the simulation $P_m \approx 0.6$, which corresponds to the steady polarized state. At $t \approx 300\,\text{s}$, the shape factor of cases D1 and D2 correspond to a circular geometry ($SF \approx 1$; see Fig. S10g). This implies that the cell geometry has little influence in the polarization process of cases D1 and D2. The results presented above suggest, as in the previous sections, that the attainment of a steady polarized state depends on the level of polarization displayed by the cell when the last stimulus vanishes. The different trends of P_Γ and P_m after $t = t_{\text{myo}}$ in case D2 (P_Γ increases whereas P_m temporarily decreases) suggest that P_Γ is the polarization factor that better accounts for the polarized state of the cell. Following this idea, we hypothesize that the P_Γ threshold for cell polarization is located between the P_Γ values of cases D1 and D2 at $t = t_{\text{myo}}$; see Fig. 10c.

5 Discussion

We developed a phase-field model of keratocyte migration to study cell polarization. The model accounts for cell deformation, the dynamics of RhoA proteins and myosin, and the forces acting on the actomyosin network. We use the wave-pinning model to capture the dynamics of RhoA proteins. The key feature of our model is the application of the wave-pinning model on a deformable geometry, in which we consider the cell membrane and the cytosol as two individual moving domains. This approach allows us to study the mechanisms of keratocyte polarization in different scenarios and the interplay between RhoA proteins, myosin-induced contraction, and cell geometry. We first study the influence of myosin activity on cell polarization. Our results show that the attainment of a steady polarized state depends on the strength of myosin down- or up-regulation. Our data also show that myosin upregulation favors cell polarization and cells with strong myosin inhibition cannot polarize or move. Our model results explain the discrepancies observed in keratocytes with down- and up-regulated myosin activity[13,20]. We hypothesize that keratocytes in ref.[13] and ref.[20] are subjected to different levels of myosin inhibition. Our results of keratocytes exposed to spatially-localized variations of myosin activity may explain why upregulated cells in ref.[20] polarize but downregulated cells do not. We hypothesize that cells in ref.[20] are subjected to low levels of myosin down- and up-regulation. Our model provides a mechanistic explanation for cell polarization induced by mechanical impact. Mechanically-stimulated cells with strong myosin inhibition are unable to polarize, which further confirms that myosin contraction is essential for cell polarization.

References[13,21] postulated that spatially-localized stimulation beyond a threshold level unbalances the non-polarized state of the cell and triggers cell polarization. We leverage the results presented in Section 4.3 (spatially-localized variations of myosin activity) and Section 4.4 (mechanical impact) to test this idea. The results confirm that, at the time the external stimuli vanish, the cell must display a minimum level of polarization to attain a polarized and motile steady state. In addition, the results suggest that the threshold level is controlled by the polarization factor P_Γ. To further investigate this hypothesis, we compute P_Γ, P_m, and SF at the time the last external stimulus vanishes, denoted as $P_\Gamma^\star$, $P_m^\star$, and $SF^\star$, for the cases presented in Sections 4.3 and 4.4. We select the cases that allow us to confirm or reject the hypothesis. The values $P_\Gamma^\star$, $P_m^\star$, and $SF^\star$ for those distinctive cases may be found in Fig. S11. We find that $P_\Gamma^\star \geq 0.13$ for all the cases in which the cell attains a steady polarized state and $P_\Gamma^\star \leq 0.1$ for all the cases in

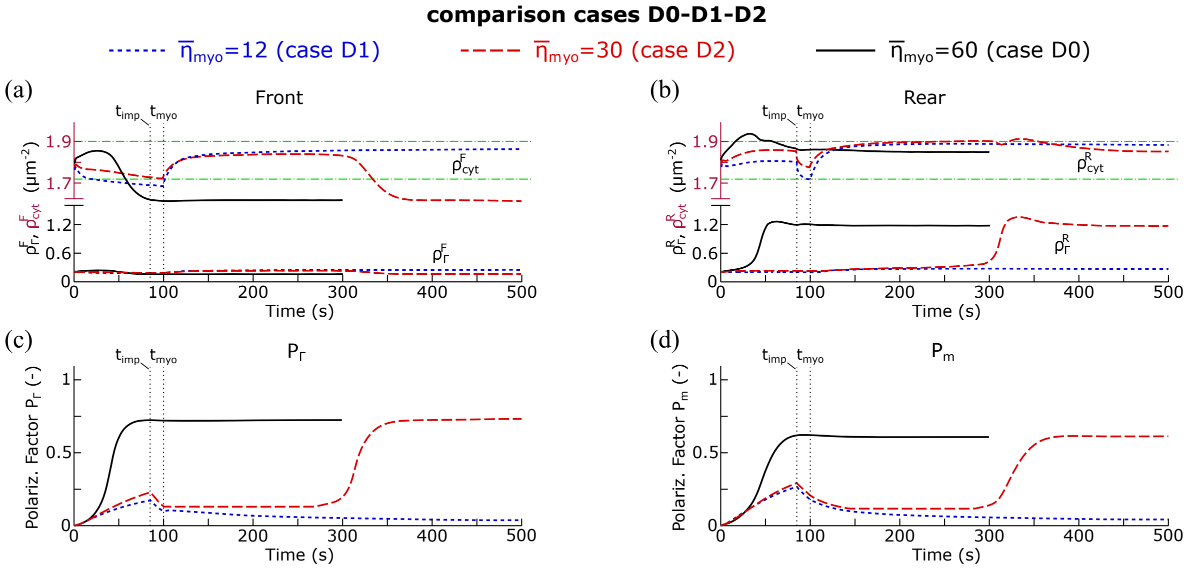

Fig. 10 Influence of myosin inhibition in cell polarization by mechanical impact. The object pushing the cell is removed at $t_{\text{imp}} = 85\,\text{s}$. Myosin activity is inhibited in the entire cell for $t_{\text{myo}} = 100\,\text{s}$. We compare two levels of myosin inhibition (cases D1 and D2) with the standard level of myosin activity (case D0). Time evolution of *(a)* ρ^F_Γ and ρ^F_{cyt}; *(b)* ρ^R_Γ and ρ^R_{cyt}; *(c)* P_Γ; and *(d)* P_m for three simulations with $\overline{\eta}_{\text{myo}} = 12$ (case D1, blue dotted line), 30 (case D2, red dashed line), and $60\,\text{pN}\mu\text{m}$ (case D0, black solid line). We stop the simulations with $\overline{\eta}_{\text{myo}} = 12$ and $30\,\text{pN}\mu\text{m}$ at $t = 600\,\text{s}$, rather than $300\,\text{s}$, so that the simulations can achieve a steady state.

which the cell does not polarize; see Fig. S11a. $P^\star_m$, however, cannot be separated in two non-overlapping sets according to the attainment of a steady polarized state; see Fig. S11b. For instance, $P^\star_m = 0.165$ (case C2) leads to cell polarization and $P^\star_m = 0.175$ (case D1) does not. Similarly to $P^\star_m$, $SF^\star$ is non-conclusive to determine persistent polarization; see Fig. S11c. Our results confirm that the threshold for cell polarization is controlled by P_Γ and is between $P_\Gamma = 0.1$ and $P_\Gamma = 0.13$. In addition, case B1 (a myosin-inhibited cell that does not attain a steady polarized state) suggests that myosin inhibition raises the P_Γ threshold for cell polarization, which supports the positive role of myosin contraction on cell polarization. All our results are consistent with the concept of a threshold level for cell polarization induced by external stimuli. Lin and collaborators observed the existence of a threshold for HeLa cells polarization determined by the spatial gradient of the active Rho GTPases[26], which supports our conclusions. We think that additional experiments and computational works might confirm the existence of the threshold and provide insight into the factors that determine the threshold level.

Our results show that there is a tight interaction between the Rho GTPases dynamics, the cell's geometry, and cell polarization. In fact, changes in the cell geometry can trigger the bistability of the Rho GTPases, which results in cell polarization. We believe that capturing the interactions between the signaling proteins and the compounds of the motile machinery in a moving cell is essential to study cell polarization. Other authors have highlighted the impact of cell shape on the dynamics of Rho GTPases[31,33]. Our work shows that changes in cell geometry are essential to understand cell polarization. In addition, our results support the theory that symmetry breaking and the initiation of motion begins at the prospective cell's rear and is driven by myosin contraction[14,20,21]. Other authors, however, observed that fibroblast polarization is driven by actin depolymerization[16]. Our model can be extended to investigate the role played by actin assembly and disassembly in cell polarization. In that case, our model should include a new module that accounts for the Rho GTPases-dependent phase transformations of the actin compounds. Likewise, a more detailed description of the adhesion proteins dynamics would shed light into the role played by adhesion in cell polarization. Finally, the incorporation of stochastic fluctuations of the actin flow into our model would permit to study spontaneous cell polarization and test the existence of a threshold level when polarization is induced by internal stimuli.

Conflicts of interest

There are no conflicts to declare.

Notes and references

1 J. E. Talmadge and I. J. Fidler, *Cancer research*, 2010, **70**, 5649–5669.
2 P. Friedl, Y. Hegerfeldt and M. Tusch, *International Journal of Developmental Biology*, 2004, **48**, 441–449.
3 V. Lecaudey and D. Gilmour, *Current opinion in cell biology*, 2006, **18**, 102–107.
4 D. J. Montell, *Science*, 2008, **322**, 1502–1505.
5 A. D. Luster, R. Alon and U. H. von Andrian, *Nature immunology*, 2005, **6**, 1182–1190.
6 J. A. Madri and D. Graesser, *Journal of Immunology Research*, 2000, **7**, 103–116.
7 I. Kaverina, O. Krylyshkina and J. V. Small, *The international journal of biochemistry & cell biology*, 2002, **34**, 746–761.
8 K. Keren, Z. Pincus, G. M. Allen, E. L. Barnhart, G. Marriott, A. Mogilner and J. A. Theriot, *Nature*, 2008, **453**, 475–480.

9 J. Lee, M. Leonard, T. Oliver, A. Ishihara and K. Jacobson, *The Journal of cell biology*, 1994, **127**, 1957–1964.
10 T. D. Pollard and G. G. Borisy, *Cell*, 2003, **112**, 453–465.
11 J. A. Theriot and T. J. Mitchison, *Nature*, 1991, **352**, 126–131.
12 C. A. Wilson, M. A. Tsuchida, G. M. Allen, E. L. Barnhart, K. T. Applegate, P. T. Yam, L. Ji, K. Keren, G. Danuser and J. A. Theriot, *Nature*, 2010, **465**, 373–377.
13 A. B. Verkhovsky, T. M. Svitkina and G. G. Borisy, *Current Biology*, 1999, **9**, 11–S1.
14 L. P. Cramer, *Nature Cell Biology*, 2010, **12**, 628–632.
15 B. Ladoux, R.-M. Mège and X. Trepat, *Trends in cell biology*, 2016, **26**, 420–433.
16 T. Mseka and L. P. Cramer, *Current Biology*, 2011, **21**, 2085–2091.
17 R. D. Mullins, *Cold Spring Harbor perspectives in biology*, 2010, **2**, a003392.
18 F. Raynaud, M. E. Ambühl, C. Gabella, A. Bornert, I. F. Sbalzarini, J.-J. Meister and A. B. Verkhovsky, *Nature Physics*, 2016, **12**, 367–373.
19 J. Xu, A. Van Keymeulen, N. M. Wakida, P. Carlton, M. W. Berns and H. R. Bourne, *Proceedings of the National Academy of Sciences*, 2007, **104**, 9296–9300.
20 P. T. Yam, C. A. Wilson, L. Ji, B. Hebert, E. L. Barnhart, N. A. Dye, P. W. Wiseman, G. Danuser and J. A. Theriot, *The Journal of cell biology*, 2007, **178**, 1207–1221.
21 E. Barnhart, K.-C. Lee, G. M. Allen, J. A. Theriot and A. Mogilner, *Proceedings of the National Academy of Sciences*, 2015, **112**, 5045–5050.
22 A. Wicki and V. Niggli, *International journal of cancer*, 2001, **91**, 763–771.
23 P. J. Van Haastert and P. N. Devreotes, *Nature reviews Molecular cell biology*, 2004, **5**, 626–634.
24 E. L. Barnhart, K.-C. Lee, K. Keren, A. Mogilner and J. A. Theriot, *PLoS biology*, 2011, **9**, year.
25 D. E. Discher, P. Janmey and Y.-l. Wang, *Science*, 2005, **310**, 1139–1143.
26 B. Lin, W. R. Holmes, C. J. Wang, T. Ueno, A. Harwell, L. Edelstein-Keshet, T. Inoue and A. Levchenko, *Proceedings of the National Academy of Sciences*, 2012, **109**, E3668–E3677.
27 H. Gomez and K. G. van der Zee, *Encyclopedia of Computational Mechanics Second Edition*, 2018, 1–35.
28 H. Gomez, M. Bures and A. Moure, *Philosophical Transactions of the Royal Society A*, 2019, **377**, 20180203.
29 A. Moure and H. Gomez, *Archives of Computational Methods in Engineering*, 2019, 1–34.
30 Y. Mori, A. Jilkine and L. Edelstein-Keshet, *Biophysical journal*, 2008, **94**, 3684–3697.
31 D. Cusseddu, L. Edelstein-Keshet, J. A. Mackenzie, S. Portet and A. Madzvamuse, *Journal of theoretical biology*, 2019, **481**, 119–135.
32 R. Diegmiller, H. Montanelli, C. B. Muratov and S. Y. Shvartsman, *Biophysical journal*, 2018, **115**, 26–30.
33 W. Giese, M. Eigel, S. Westerheide, C. Engwer and E. Klipp, *Physical biology*, 2015, **12**, 066014.
34 A. Moure and H. Gomez, *Biomechanics and Modeling in Mechanobiology*, 2020, 1–18.
35 D. Shao, H. Levine and W.-J. Rappel, *Proceedings of the National Academy of Sciences*, 2012, **109**, 6851–6856.
36 C. W. Wolgemuth, J. Stajic and A. Mogilner, *Biophysical journal*, 2011, **101**, 545–553.
37 A. F. Marée, V. A. Grieneisen and L. Edelstein-Keshet, *PLoS computational biology*, 2012, **8**, year.
38 B. Vanderlei, J. J. Feng and L. Edelstein-Keshet, *Multiscale Modeling & Simulation*, 2011, **9**, 1420–1443.
39 T. Biben and C. Misbah, *Physical Review E*, 2003, **67**, 031908.
40 T. Biben, K. Kassner and C. Misbah, *Physical Review E*, 2005, **72**, 041921.
41 X. Li, J. Lowengrub, A. Rätz and A. Voigt, *Communications in mathematical sciences*, 2009, **7**, 81.
42 K. E. Teigen, X. Li, J. Lowengrub, F. Wang and A. Voigt, *Communications in mathematical sciences*, 2009, **4**, 1009.
43 D. Michaelson, J. Silletti, G. Murphy, P. D'Eustachio, M. Rush and M. R. Philips, *The Journal of cell biology*, 2001, **152**, 111–126.
44 A. A. Schmitz, E.-E. Govek, B. Böttner and L. Van Aelst, *Experimental cell research*, 2000, **261**, 1–12.
45 K. F. Swaney, C.-H. Huang and P. N. Devreotes, *Annual review of biophysics*, 2010, **39**, 265–289.
46 A. J. Ridley, *Journal of cell science*, 2001, **114**, 2713–2722.
47 A. J. Ridley, M. A. Schwartz, K. Burridge, R. A. Firtel, M. H. Ginsberg, G. Borisy, J. T. Parsons and A. R. Horwitz, *Science*, 2003, **302**, 1704–1709.
48 Y. Mori, A. Jilkine and L. Edelstein-Keshet, *SIAM journal on applied mathematics*, 2011, **71**, 1401–1427.
49 G. R. Walther, A. F. Marée, L. Edelstein-Keshet and V. A. Grieneisen, *Bulletin of mathematical biology*, 2012, **74**, 2570–2599.
50 B. Rubinstein, M. F. Fournier, K. Jacobson, A. B. Verkhovsky and A. Mogilner, *Biophysical journal*, 2009, **97**, 1853–1863.
51 M. Nickaeen, I. L. Novak, S. Pulford, A. Rumack, J. Brandon, B. M. Slepchenko and A. Mogilner, *PLoS computational biology*, 2017, **13**, e1005862.
52 P. B. Canham, *Journal of theoretical biology*, 1970, **26**, 61–81.
53 W. Helfrich, *Zeitschrift für Naturforschung C*, 1973, **28**, 693–703.
54 A. Moure and H. Gomez, *Computer Methods in Applied Mechanics and Engineering*, 2017, **320**, 162–197.
55 W. Marth and A. Voigt, *Journal of mathematical biology*, 2014, **69**, 91–112.
56 T. J. Hughes, J. A. Cottrell and Y. Bazilevs, *Computer methods in applied mechanics and engineering*, 2005, **194**, 4135–4195.
57 Y. Bazilevs, V. M. Calo, J. A. Cottrell, J. A. Evans, T. J. R. Hughes, S. Lipton, M. A. Scott and T. W. Sederberg, *Computer Methods in Applied Mechanics and Engineering*, 2010, **199**, 229–263.
58 Y. Bazilevs, C. Michler, V. Calo and T. Hughes, *Computer Methods in Applied Mechanics and Engineering*, 2010, **199**, 780–790.

59 J. Cottrell, T. Hughes and A. Reali, *Computer methods in applied mechanics and engineering*, 2007, **196**, 4160–4183.

60 H. Gomez and L. De Lorenzis, *Computer Methods in Applied Mechanics and Engineering*, 2016, **309**, 152–181.

61 D. Schillinger, L. Dede, M. A. Scott, J. A. Evans, M. J. Borden, E. Rank and T. J. Hughes, *Computer Methods in Applied Mechanics and Engineering*, 2012, **249**, 116–150.

62 R. Schmidt, R. Wüchner and K.-U. Bletzinger, *Computer Methods in Applied Mechanics and Engineering*, 2012, **241**, 93–111.

63 M. A. Scott, D. C. Thomas and E. J. Evans, *Computer Methods in Applied Mechanics and Engineering*, 2014, **269**, 222–264.

64 Z. Petrášek, C. Hoege, A. Mashaghi, T. Ohrt, A. A. Hyman and P. Schwille, *Biophysical journal*, 2008, **95**, 5476–5486.

65 S. B. Marston, *Biochemical Journal*, 1982, **203**, 453–460.

66 A. R. Bausch, F. Ziemann, A. A. Boulbitch, K. Jacobson and E. Sackmann, *Biophysical journal*, 1998, **75**, 2038–2049.

67 A. Moure and H. Gomez, *Biomechanics and modeling in mechanobiology*, 2018, **17**, 1243–1268.

68 J.-Y. Tinevez, U. Schulze, G. Salbreux, J. Roensch, J.-F. Joanny and E. Paluch, *Proceedings of the National Academy of Sciences*, 2009, **106**, 18581–18586.

69 T. Oliver, M. Dembo and K. Jacobson, *The Journal of cell biology*, 1999, **145**, 589–604.

70 J. Chung and G. Hulbert, *Journal of applied mechanics*, 1993, **60**, 371–375.

71 K. E. Jansen, C. H. Whiting and G. M. Hulbert, *Computer methods in applied mechanics and engineering*, 2000, **190**, 305–319.

72 L. Dalcin, N. Collier, P. Vignal, A. Côrtes and V. Calo, *Computer Methods in Applied Mechanics and Engineering*, 2016, **308**, 151–181.

73 S. Balay, S. Abhyankar, M. F. Adams, J. Brown, P. Brune, K. Buschelman, L. Dalcin, A. Dener, V. Eijkhout, W. D. Gropp, D. Karpeyev, D. Kaushik, M. G. Knepley, D. A. May, L. C. McInnes, R. T. Mills, T. Munson, K. Rupp, P. Sanan, B. F. Smith, S. Zampini, H. Zhang and H. Zhang, *PETSc Web page*, 2019, `https://www.mcs.anl.gov/petsc`.

74 R. Shimoni, M. Y. Kim Pham, M. J. Ludford-Menting, M. Gu and S. M. Russell, *PloS one*, 2014, **9**, year.

75 F. Ziebert, S. Swaminathan and I. S. Aranson, *Journal of The Royal Society Interface*, 2012, **9**, 1084–1092.